POLITECNICO
MILANO 1863

A depth-integrated model for debris flow propagation by adopting SPH method

M.Sc. Thesis of
Seyed Ali Mousavi Tayebi

Supervisor:
Dr. Andrea Galli

Co-supervisor:
Dr. Manuel Pastor Pérez

Programme:
Civil Engineering for Risk Mitigation

School of Civil, Environmental and
Land Management Engineering
Politecnico di Milano

Seyed Ali Mousavi Tayebi
A depth-integrated model for debris flow propagation by adopting SPH method
2023

Contents

Contents

List of Figures

List of Figures

Abstract

Debris flows are complex natural phenomena that cause significant economic damage and casualties in mountainous regions and along rivers. Accurate and efficient debris flow analysis is crucial for assessing risks and identifying vulnerable areas that require mitigation measures. This study presents an advanced numerical modeling approach to simulate debris flows, focusing on the integration of excess pore-water pressure for a better analysis.

The proposed model implements a two-phase model and provides evolution of excess pore pressure. The mathematical approach is a depth integrated model, which can reproduce debris flow propagation with soil permeability ranging from high to low. The equations are discretized using the Smooth Particle Hydrodynamic (SPH) technique, featuring a double set of nodes for solid and fluid particles.

The SPH depth integrated model is a 2D model capable of predicting runout distance, flow velocity, deposition pattern, and final volume of debris flows. It is based on a coupled depth integrated model derived from a velocity-pressure version of Biot-Zienkiewicz equations, and uses constitutive or rheological models such as the frictional and Bingham models to simulate debris flows. A case study validated the model through back-analysis.

The performance and limitations of the proposed model are assessed using benchmark exercises, including dam break problems and real-case scenarios with reliable information. The validation analysis demonstrates that the model can accurately reproduce debris flow propagation velocity, runout distance, and deposit thickness, and effectively model the time-space evolution of excess pore-water pressures throughout the propagation stage.

In conclusion, the advanced numerical modeling approach presented in this study offers significant improvements in debris flow analysis, specifically by integrating more precise excess pore-water pressure description as well as providing erosion simulation. This enhanced model can help decision-makers and practitioners in assessing and managing risks associated with debris flows, ultimately contributing to the protection of lives and infrastructure in vulnerable areas.

Sommario

Le colate di detriti sono fenomeni naturali complessi che causano ingenti danni economici e vittime nelle regioni montuose e lungo i fiumi. Un'analisi accurata ed efficiente delle colate di detriti è fondamentale per valutare i rischi e individuare le aree vulnerabili che richiedono misure di mitigazione. Questo studio presenta un avanzato approccio di modellazione numerica per simulare le colate di detriti, concentrandosi sull'integrazione della pressione interstiziale in eccesso per una migliore analisi.

Il modello proposto implementa un modello a due fasi e fornisce l'evoluzione della pressione interstiziale in eccesso. L'approccio matematico è un modello integrato in profondità, in grado di riprodurre la propagazione delle colate di detriti con permeabilità del suolo che varia da alta a bassa. Le equazioni sono discretizzate utilizzando la tecnica Smooth Particle Hydrodynamic (SPH), caratterizzata da un doppio insieme di nodi per particelle solide e fluide.

Il modello SPH integrato in profondità è un modello 2D in grado di prevedere la distanza di esaurimento, la velocità del flusso, il modello di deposizione e il volume finale delle colate di detriti. Si basa su un modello integrato in profondità accoppiato derivato da una versione di velocità-pressione delle equazioni di Biot-Zienkiewicz e utilizza modelli costitutivi o reologici come i modelli frizionali e di Bingham per simulare le colate di detriti. Un caso di studio ha validato il modello attraverso un'analisi retrospettiva.

Le prestazioni e i limiti del modello proposto sono valutati utilizzando esercizi di riferimento, tra cui problemi di rottura di dighe e scenari reali con informazioni affidabili. L'analisi di validazione dimostra che il modello può riprodurre con precisione la velocità di propagazione delle colate di detriti, la distanza di esaurimento e lo spessore del deposito, e modellare efficacemente l'evoluzione spazio-temporale delle pressioni interstiziali in eccesso durante la fase di propagazione.

In conclusione, l'avanzato approccio di modellazione numerica presentato in questo studio offre miglioramenti significativi nell'analisi delle colate di detriti, in particolare integrando una descrizione più precisa della pressione interstiziale in eccesso e fornendo una simulazione dell'erosione. Questo modello migliorato può aiutare i responsabili delle decisioni e i professionisti nella valutazione e nella gestione dei rischi associati alle colate di detriti, contribuendo in ultima analisi alla protezione delle vite e delle infrastrutture nelle aree vulnerabili.

Acknowledgments

First of all, I would like to thank my thesis directors Andrea Galli and Manuel Pastor for their unwavering guidance and support. I also thank you for giving me the opportunity to start my research career in your department. Your patience, understanding and friendship allowed me to carry out this investigation, and your advice, constructive comments and availability facilitated the completion of this M.Sc. thesis.

I must also thank my dearest friends AliHossein, Mohammad, Mahdi, and Mehrad for their support, sympathy and all the happy memories we shared. Many thanks to Sina and Sina Kian for being my friends and making this experience so much fun. For all the above and much more you can always count on my deepest friendship.

Finally, I would like to express my deepest appreciation to my father (Mahdi), mother (Souri) and brother (Saeid) for believing in me and always being my most reliable supporters. I dedicate this thesis to my family for their enormous sacrifices, endless love and encouragement.

Milano, 01 Jun 2023   Seyed

1 Introduction

1.1 Background

A landslide, also referred to as a landslip, is a hazardous event which puts together various types of ground instability, like rockfalls, deep slope failures, and shallow debris flows. These can take place in offshore, coastal, or onshore settings. While gravity is the primary cause of a landslide, other elements also play a role in impacting the initial stability of the slope.

Normally, pre-existing factors lead to certain sub-surface conditions that make the area or slope susceptible to failure. The actual landslide, however, usually requires a trigger to start it. The stages of landslide events can be broken down into three parts (fig. 1.1):

1. **Initiation:** In this phase the initial mass is released.

2. **Propagation:** In this phase the mass flows along the travel path.

3. **Deposition:** In this phase the mass stops and is deposited on a colluvial fan [17].

Figure 1.1: Landslide of Tessina Valley on the Bellunese edge of the Alps (1960)

1.1.1 Initiation

The initiation of landslides holds significant relevance as the magnitude of such events hinges on the volume set in motion. Landslides are usually caused by slope instability, but one or more triggering factors can usually be identified as:

- **Geological**: Sheared materials, permeability contrasts, jointed or fissured materials, earthquakes, etc.

- **Morphological**: Slope angle, erosion, slope loading, etc.

- **Physical**: Heavy rainfall, rapid snow melt, volcanic eruption, ground water changes, soil pore water pressure, etc.

- **Human**: Excavation, loading, mining, deforestation, water management, etc.

In the majority of cases the main initiator of landslides is heavy or prolonged rainfall. Typically, this takes the form of either an exceptional short-lived event or a long-duration rainfall event of low intensity. A very high rate of rainfall is necessary in the former case, whereas in the latter, a moderate rainfall intensity may be sufficient; what is critical is the duration and existing pore water pressure conditions. Figure 1.2 shows heavy rain that triggered floods and landslides which cut roads in San Martino in Badia, Italy, 05 August 2022.

Figure 1.2: Landslides in San Martino in Badia, Italy, (2022)[10]

Constitutive models are capable to describe solid behavior up to failure during the triggering stage. To this day, many physically based methods based on these models

have been proposed to provide landslide susceptibility analysis. Figure 1.3 illustrates a landslide susceptibility map computed with r.slope.stability code in the La Arenosa catchment, northern Colombian Andes.
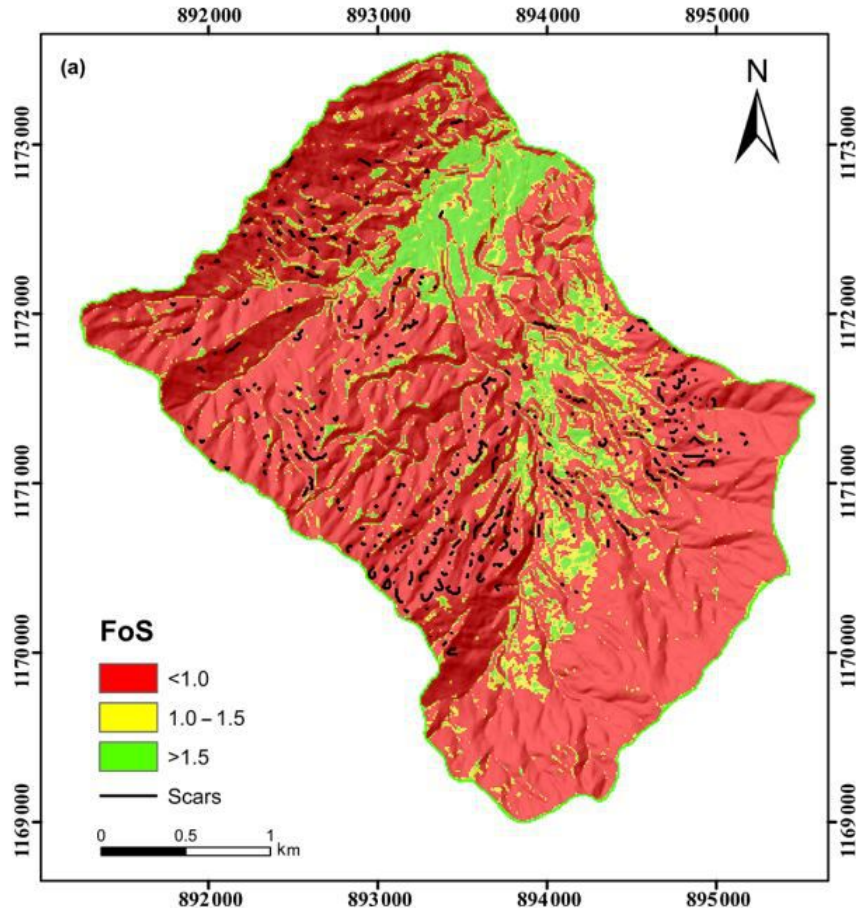
Figure 1.3: Landslide susceptibility map computed with r.slope.stability[29]

1.1.2 Propagation

In planning infrastructure and residential locations, it is essential to study propagation up to deposition. When soil has been liquefied or fluidized, propagation occurs, in other words, the soil behaves like a fluid. Currently, no satisfactory constitutive model has been developed that can fully describe the behavior of soil mixtures under the full range of strain rates present in a rapid landslide (from its initiation to deposition, passing through its propagation). Rheological models have traditionally been used to describe the propagation of flowing masses due to the fluid-like nature of this behavior. On Lantau Island, Hong Kong, a real landslide occurred on Yu Tung Road (fig. 1.4(a)). A particle-based meshless method implementing rheological models was used to simulate this event (fig. 1.4(b)).
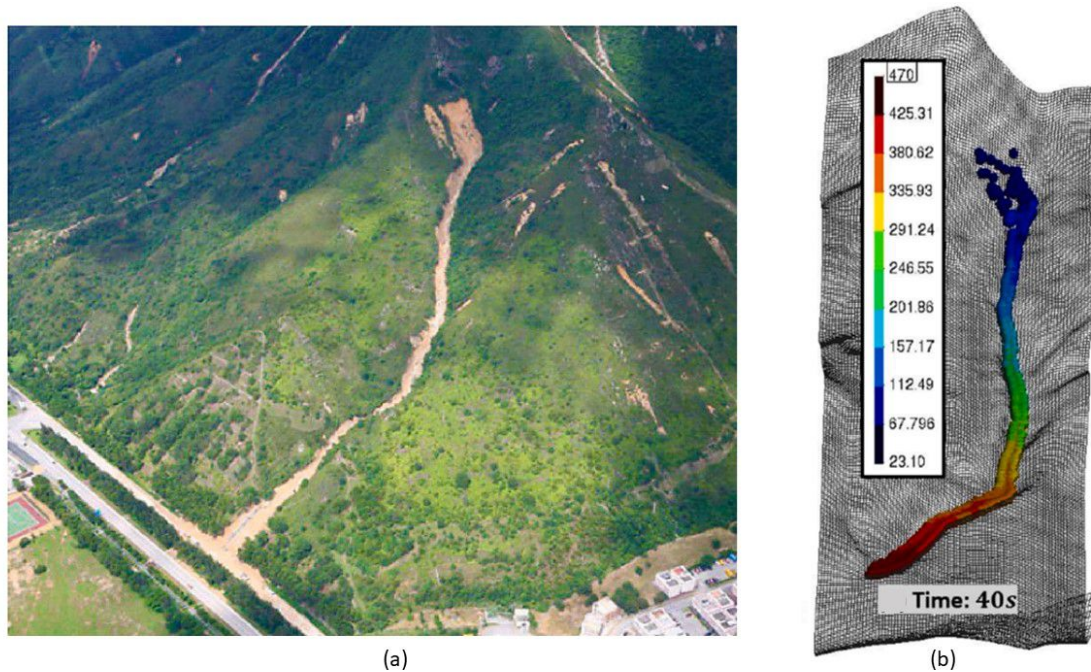
Figure 1.4: Yu Tung debris flow on a hillside in Lantau Island, Hong Kong (a)Aerial
View of the debris flow event (b)Debris flow numerical simulation[39]

1.1.3 Types and Classification

Landslides can be identified by a number of criteria, including the failure mechanisms,
nature of the materials, propagation, and other parameters such as geomorphological
features, slope geometry, and climate. One of the most used classifications for landslides
is the Varnes classification (1978). The landslide classification based on Varnes' system
is composed of two terms:

1. **Material**

2. **Movement**

The material types used in the various schemes are rock, soil, earth, mud and debris,
classified as follows:

- **Rock:** A dense or firm mass that was intact and in its natural place before move-
  ment began.

- **Soil:** An aggregate of solid particles, generally of minerals and rocks, that either
  was transported or formed by the weathering of rock in place.

- **Earth:** Material in which 80% or more of the particles are smaller than 2mm, the
  upper limit of sand-sized particles.

- **Mud:** Material in which 80% or more of the particles are smaller than 0.06mm, the upper limit of silt-sized particles.

- **Debris:** Contains a significant proportion of coarse material; 20% to 80% of the particles are larger than 2mm, and the remainder are less than 2mm.

There are five distinct kinematical types of movement [41]:

- **Falls**

- **Topples**

- **Slides**

- **Spreads**

- **Flows**

Combining materials and types of movements, classification terms will appear like those given in table 1.1.

1.1.4 Fluid phase and consolidation

Consolidation is another significant aspect of some types of flows. This is when excess pore pressure is dissipated or generated and as a result, mixture dynamics are affected. It is worth mentioning that another classification can also be defined based on characteristic times, i.e. propagation time (t_p) and consolidation time (t_c) for different types of materials. These characteristic times will also determine the number of phases to consider and whether to take into account the effect of excessive pore-water pressure. Table 1.2 shows different categories based on this classification. In the following, each class will be briefly discussed.

When rock avalanches occur, solid blocks become disintegrated into smaller pieces as they gain speed. The discrete element model (DEM) is particularly well suited for modeling granular flows, such as rock avalanches, which contain fragments of different sizes and shapes. However, the model generally takes a considerable amount of time to compute. Therefore, continuum models are frequently used here, using a **one-phase** granular fluid. On December 9th 2022 the devastating impact force of the stones detached from Monte Due Mani next to Lecco-Ballabio road, tore apart the protection nets installed at the top of the tunnel and destroyed the retaining wall (fig. 1.5)[5].

The **two-phase** models can be applied to saturated granular flows such as rock avalanches where the permeability is high enough so that the consolidation time is much shorter than the time of propagation, and the material behaves as drained. In this case solid particles and water can have different velocities, therefore, models must include the velocities of both solid and fluid phases.

Table 1.1: Varnes' classification of slope movement (1978)

Models	Types	Characteristic	Characteristic Time	Permeability
One-phase	Unsaturated granular flows Dry rock avalanches	Flow of fragmented rock	t_p	High/Low
Two-phase	Saturated granular flows Wet rock avalanches	Mixtures of fine soil particles and water	$t_c \ll t_p$	High
One-phase+Pwp	Mudflows	Mixtures of soil particles and water, with small relative displacements	$t_c \gg t_p$	Low
Two-phase+Pwp	Debris flows	Flow of partially or fully saturated debris	$t_c \cong t_p$	Medium

Table 1.2: Types of flows

Figure 1.5: Rock avalanche on Lecco-Ballabio road [11]

A mudflow is a mixture of fine soil particles and water, with a viscoplastic behavior. They can be modeled with continuum models using **one-phase** viscous fluids. Since permeability is very low in mudflows, the excessive pore-water pressure dissipation time is much higher than the propagation time. Therefore, flow behavior can be assumed to be undrained and **excessive pore-water pressure** must be considered. Figure 1.6 displays an event at Casamicciola in Italy where mudflows are visible, also indicating that typically, mudflows have a high run-out distance due to the significant effect of pore-water pressures [12].

Figure 1.6: The mudflow at Casamicciola in Italy (2022)

Debris flows are a mixture of water and/or air with high concentrations and sediments (rocks, gravel, clay and organic material) that have medium permeability. Debris flows can travel at extremely rapid velocities, and their debris mass moves long distances as a result of the presence of excess pore-water pressures at the propagation stage. The propagation and consolidation times in such cases are very close. Therefore, quantitative modeling of excess pore pressure time-space evolution and flow propagation is essential to assessing these hazards. From the modeling point of view, debris flows are a more complex phenomenon, as both solid particles and water can have different velocities and the stresses acting on them are needed to be involved. As a result, a **two-phase model considering excessive pore-water pressure** can be applied in these cases. Figure 1.7 depicts a debris flow that occurred in the South Tyrol region, Italy in 2022 in which different phases can be observed.

Figure 1.7: Debris flow damage in South Tyrol region [10]

1.2 Motivation

This study focuses on debris flows. Debris flows are among the most destructive and unpredictable geological phenomena, posing a significant risk to human lives, infrastructures, and the natural environment (fig. 1.8). They are typically triggered by extreme weather conditions, such as intense or prolonged rainfall and rapid snow melting. The increasing frequency and intensity of such extreme weather events, driven by climate change, further exacerbate debris flow hazards. In order to mitigate these risks and protect lives and properties, it is crucial to develop accurate and reliable predictive models that can simulate the dynamics and complicated behavior of these natural disasters. Accordingly, two-phase modeling will be applied to consider both solid and fluid phases, and their mutual interaction.

Traditional simulation approaches, such as the Finite Element Method (FEM), have proven useful in many applications but face challenges when dealing with large deformations. Meshless or mesh-free methods, which discretize space into particles without relying on fixed connectivity, have emerged as promising alternatives to address these

challenges. During the past decade, an expert research team in Madrid has developed the simulation model presented in this thesis. The model is named GeoFlow SPH and has previously been applied to theoretical, experimental, and real case histories [44]. It is based on rational continuum models which can be used to solve a variety of problems. Rational methods are based on mathematical models, usually expressed by partial differential equations. Empirical methods are used to estimate travel distances rather than providing quantitative values such as velocity. The advantage of continuum models is that they can consider the coupling of mechanical and hydraulic behavior in the model. In contrast, discrete models are better suited for cases where the granularity of the moving mass is critical, such as rock avalanches [27].

Figure 1.8: Debris flow that broke through the structure of the Fiumelatte road and railway tunnel in Varenna, Italy, (2023)

1.3 Objectives

The primary goal of this M.Sc. thesis is to examine and critically discuss a two-phase Smoothed Particle Hydrodynamics (SPH) depth integrated model, which can effectively simulate the behavior of debris flows and landslides in various geological and climatic conditions [34]. The specific objectives of the study are as follows:

    i. To integrate the principles of meshless methods and SPH to develop a robust and

accurate numerical model capable of simulating debris flows and landslides with large deformations.

  ii. To investigate the effects of pore-water pressures and bed entrainment on the dynamics and behavior of debris flows, and incorporate these factors into the developed model.

 iii. To analyze and evaluate the performance of the two-phase SPH depth integrated model and compare its effectiveness against a real-world case study.

 iv. To provide insights and recommendations for the implementation of effective countermeasures and mitigation strategies in areas prone to debris flows and landslides.

1.4 Scope of the Work

This research will primarily focus on the implementation and validation of the two-phase SPH depth integrated model, which will be applied to simulate various scenarios of debris flows and landslides. The model's performance will be assessed through a series of numerical simulations, and comparisons with real-world case studies. Furthermore, the study will investigate the potential of various debris flow countermeasures, such as screens, in reducing the destructive impact of these natural disasters on infrastructure and human lives.

1.5 Research Methodology

The research methodology employed for this investigation can be described as follows:

  a. Reviewing existing literature on debris-flow phenomena, associated mitigation strategies, and computational modeling of debris-flow.

  b. A study of common constitutive/rheological models and investigating their parameters and behaviours.

  c. Performing a computational modeling study by evaluating the screen's performance and assessing it in a real-world debris-flow scenario.

To provide a comprehensive overview of the research methodology, a workflow diagram is displayed in figure 1.9.
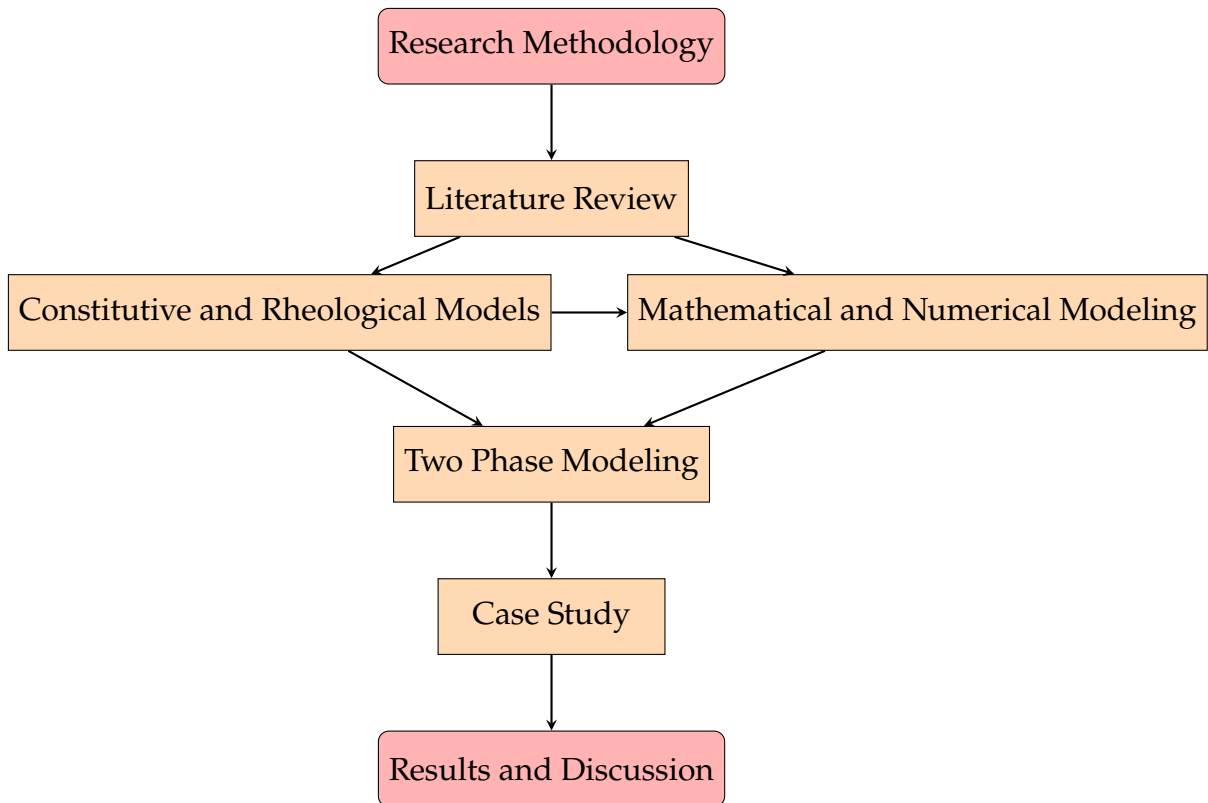
Figure 1.9: Flowchart describing the research methodology

1.6 Structure of the Work

In accordance with the mentioned objectives, the thesis is structured as follows:

Chapter 1 serves as the introduction, initially providing a brief overview of the landslide phenomenon and its fundamental aspects. Subsequently, various landslide types and their characteristics are concisely discussed, focusing on their relevant numerical modeling. The final section introduces the predictive tools and models that will be employed in this study to simulate the rapid landslide propagation.

Chapter 2 is devoted to presenting alternative mathematical models and the numerical discretization methods employed in this study. The chapter starts with basic concepts and theorems of continuum mechanics and the general mathematical model, based on Biot equations. Subsequently, the specialized mathematical model is derived from the Zienkiewicz-Shiomi model, and its governing equations are integrated along depth for an optimal balance between accuracy and computational effort. Next, the depth-integrated mathematical model is discretized using the Smoothed Particle Hydrodynamics Method (SPH). The chapter concludes with the presentation of a propagation-consolidation model that assumes interstitial pressure evolution occurs solely along the depth. Then, the consolidation equation is discretized with the Finite Difference Method (FDM) in each time step to account for excess pore pressure evolution.

Chapter 3 introduces the general framework for constitutive and rheological models. Optimal expressions for basal friction forces are determined through various rheological laws. These expressions are then utilized to complete the mathematical equations, which have been detailed in Chapter 2. Finally, to better understand and compare different constitutive and rheological models, some parametrical and sensitivity analyses will be conducted.

Chapter 4 is devoted to presenting two-phase models capable of describing the coupling between the solid skeleton and pore fluids. Initially, the effect of soil stiffness and permeability will be discussed. The chapter concludes by performing several analyses to assess drainage screens' efficacy at different consolidation rates, and simultaneously, provide excess pore pressure evolution for better insight.

Chapter 5 showcases a real-life example, assessing the proposed model's ability to replicate natural debris flows. Moreover, a simple erosion law is implemented to represent the bed entrainment phenomenon. Ultimately, the results are displayed, analyses are provided, and mitigation measures are suggested.

Chapter 6 serves as the thesis' concluding chapter, summarizing its contributions and highlighting the key points.

2 Mathematical and Numerical Modeling

2.1 Introduction

Various computational tools have been created to simulate mass flow in order to estimate characteristics of debris-flow movement, such as: velocity, height, impact force, run-out distance, and flow dispersion. These tools can be one-dimensional (1D) or quasi-three-dimensional (quasi-3D), which means they are essentially two-dimensional (2D) with an averaged third dimension, and they utilize distinct basal rheological laws based on appropriate flow behavior (shear stress versus shear rate) [44]. Some examples of these models include RAMMS::DEBRIS FLOW [7], DAN3D [21], Flo-2D [28], MassMov2D [2], r.avaflow [22], and GeoFlow SPH [32]. Since the propagation stage of debris flow is largely influenced by the spatiotemporal evolution of interstitial pore-water pressure [6], and the selected mesh-type debris flow countermeasure focuses on dissipating this pressure, the choice of a computational tool depends on the model's ability to accurately represent this particular aspect of debris flow. The GeoFlow SPH-FD model for debris flow propagation is deemed suitable because of its ability to simulate the development of pore-fluid pressure throughout the flow progression [30, 6]. The following sections detail the assumptions and formulations used in the depth integrated two phase framework, as discussed in the article by Pastor et al. (2021).

2.2 Mathematical model

A mathematical model, such as the Biot equations, can be used to explain physical phenomena in porous media, including the propagation of landslides. In landslides, fluidized geomaterials are mixtures of solid particles and pore fluids, and their interactions are crucial. This study uses mixture theory to describe this coupling, defining porosities, densities, and partial stresses for all constituents [27].

2.2.1 Materials

We will presume that the fluidized soil is comprised of a solid skeleton and a fluid phase, forming a two-phase system. In this system, the fluid fully saturates the voids (hence, the saturation ratio $S_r = 1$) as shown in fig. 2.1. The terms will be distinguished by using the subscript s for the solid component and w for the fluid phase. The densities of the two materials will be denoted by ρ_s and ρ_w. A phase density is defined as the mass of components per unit volume of a mixture, as follows:
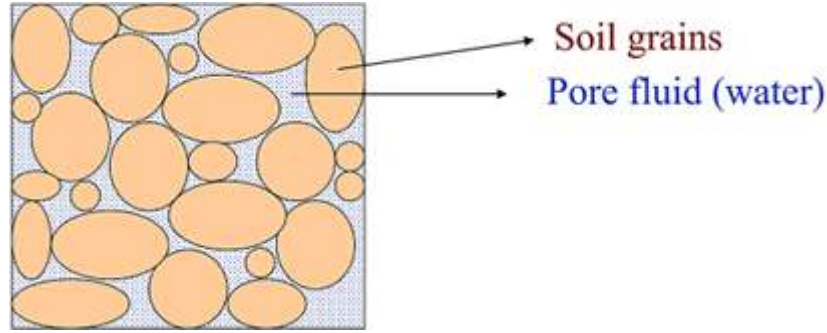
Figure 2.1: Two-phase scheme

$$\rho^{(s)} = (1 - n)\,\rho_s$$
$$\rho^{(w)} = n\rho_w \tag{2.1}$$

It is assumed that the velocities of the two phases may differ. As a result, the mathematical models that describe the balance of mass and momentum for each phase use derivatives following the solid $\frac{d^{(s)}}{dt}$ and the fluid $\frac{d^{(w)}}{dt}$ as follows:

$$\frac{d^{(s)}}{dt} = \frac{\partial}{\partial t} + v_s{}^\mathsf{T}.\mathrm{grad}$$
$$\frac{d^{(w)}}{dt} = \frac{\partial}{\partial t} + v_w{}^\mathsf{T}.\mathrm{grad} \tag{2.2}$$

where v_s and v_w are the velocities of solid and fluid particles in the mixture. The derivatives are related by the following equation:

$$\frac{d^{(w)}}{dt} = \frac{d^{(s)}}{dt} + (v_w - v_s)^\mathsf{T}.\mathrm{grad} \tag{2.3}$$

Darcy's velocity (w) can be expressed as:

$$v_w = v_s + \frac{w}{n} \tag{2.4}$$

By substituting eq. (2.4) into eq. (2.3) we can obtain the relationship between material derivatives in the two phases:

$$\frac{d^{(w)}}{dt} = \frac{d^{(s)}}{dt} + \frac{w^\mathsf{T}}{n}.\mathrm{grad} \tag{2.5}$$

2.2.2 Stresses

Stresses in the phases are related to the total stress (Cauchy) in the mixture (referred to as σ) as follows:

$$\sigma = (1 - n)\,\sigma_s + n\sigma_w$$
$$= \sigma^{(s)} + \sigma^{(w)} \tag{2.6}$$

where the partial stresses $\boldsymbol{\sigma}^{(s)}$ and $\boldsymbol{\sigma}^{(w)}$ can be defined as:

$$\begin{aligned}\boldsymbol{\sigma}^{(s)} &= (1-n)\,\boldsymbol{\sigma}_s \\ \boldsymbol{\sigma}^{(w)} &= n\boldsymbol{\sigma}_w\end{aligned} \tag{2.7}$$

In the case of the fluid, if we consider $\boldsymbol{\tau}_w$ as the deviatoric stress, p_w as the pore pressure and $\mathbf{I}$ as the second order identity tensor, we will be able to express the fluid stress as:

$$\boldsymbol{\sigma}^{(w)} = -np_w\mathbf{I} + n\,\boldsymbol{\tau}_w \tag{2.8}$$

The negative sign in the first term of equation 2.8 is due to compressive stresses. From now on, we can make the simplifying yet realistic assumption of inviscid pore fluid, i.e. shear stress is zero in the fluid phase. Accordingly, the total stress will be:

$$\boldsymbol{\sigma} = \boldsymbol{\sigma}^{(s)} - np_w\mathbf{I} + n\,\boldsymbol{\tau}_w \tag{2.9}$$

Additionally, for inviscid pore fluids, we can formulate the effective stress used in Soil Mechanics as follows:

$$\boldsymbol{\sigma}' = \boldsymbol{\sigma} + p_w\mathbf{I} = (1-n)\,(\boldsymbol{\sigma}_s + p_w\mathbf{I}) \tag{2.10}$$

Furthermore, it can be related to the solid partial stress as follows:

$$\boldsymbol{\sigma}^{(s)} = \boldsymbol{\sigma}' - (1-n)\,p_w\mathbf{I} \tag{2.11}$$

Finally, the partial stresses can be expressed as:

$$\boldsymbol{\sigma}^{(s)} = \boldsymbol{\sigma}' - (1-n)\,p_w\mathbf{I} \tag{2.12}$$

$$\boldsymbol{\sigma}^{(w)} = -np_w\mathbf{I} \tag{2.13}$$

2.2.3 Conservation of mass

The balance of mass equations for the mixture can be formulated as:

$$\begin{aligned} -\frac{d^{(s)}n}{dt} + (1-n)\operatorname{div}\boldsymbol{v}_s &= 0 \\ \frac{1}{Q}\frac{d^{(w)}p_w}{dt} + \frac{d^{(w)}n}{dt} + n\operatorname{div}\boldsymbol{v}_w &= 0 \end{aligned} \tag{2.14}$$

In which Q is the mixed volumetric stiffness and depends on volumetric stiffnesses of solid grains and water:

$$\frac{1}{Q} = \frac{(1-n)}{K_s} + \frac{n}{K_w} \approx \frac{n}{K_w} \tag{2.15}$$

If we sum up the mass balance equations for each phase, we can obtain:

$$\frac{1}{Q}\frac{d^{(w)}p_w}{dt} + \frac{d^{(w)}n}{dt} - \frac{d^{(s)}n}{dt} + (1-n)\operatorname{div}\boldsymbol{v}_s + n\operatorname{div}\boldsymbol{v}_w = 0 \tag{2.16}$$

Finally, if we take into account equation 2.5, we arrive to:

$$\frac{1}{Q}\frac{d^{(w)}p_w}{dt} + \operatorname{div}\boldsymbol{w} + \operatorname{div}\boldsymbol{v}_s = 0 \tag{2.17}$$

2.2.4 Conservation of momentum

The balance of momentum equations for the fluid and solid phases can be written as:

$$n\rho_w\frac{d^{(w)}\boldsymbol{v}_w}{dt} = \left\{-n\operatorname{grad}p_w\right\} + n\rho_w\boldsymbol{b} - \boldsymbol{R} \tag{2.18}$$

$$(1-n)\,\rho_s\frac{d^{(s)}\boldsymbol{v}_s}{dt} = \begin{cases} \operatorname{div}\boldsymbol{\sigma}^{(s)} - p_w\operatorname{grad}n & \text{(a)} \\ \operatorname{div}\boldsymbol{\sigma} + n\operatorname{grad}p_w & \text{(b)} \\ \operatorname{div}\boldsymbol{\sigma}' - (1-n)\operatorname{grad}p_w & \text{(c)} \end{cases} + (1-n)\,\rho_s\boldsymbol{b} + \boldsymbol{R} \tag{2.19}$$

where $\boldsymbol{b}$ is the vector of body forces, $\boldsymbol{R}$ is the interaction solid-fluid forces. If we define $\boldsymbol{R}_{(\alpha)}$ as the interaction force acting on phase (α), we obtain:

$$\boldsymbol{R} = -n\boldsymbol{R}_w = (1-n)\,\boldsymbol{R}_s \tag{2.20}$$

2.2.5 Interaction laws

The Interaction law is a fundamental concept that governs the coupling between solid and fluid. Here we introduce Anderson and Jackson law [1] which is a coupling law used by Pitman and Le [36]. This law is suitable for a wide range of porosities, and when the relative velocity is larger:

$$\boldsymbol{R} = \frac{n(1-n)}{V_T n^m}(\rho_s - \rho_w)\,g\,(\boldsymbol{v}_w - \boldsymbol{v}_s) \tag{2.21}$$

where V_T is the terminal velocity of solid particles falling in the fluid, g the acceleration of gravity and m a constant.

Please note that in both cases, we can express the interaction term as:

$$\boldsymbol{R} = C_d\,(\boldsymbol{v}_w - \boldsymbol{v}_s) \tag{2.22}$$

where C_d is:

$$C_d = \frac{n(1-n)}{V_T n^m}(\rho_s - \rho_w)\,g \tag{2.23}$$

Other laws can also be written in this form, C_d being dependent on $(\boldsymbol{v}_w - \boldsymbol{v}_s)$.

The balance equations of mass and momentum for the mixture described above have to be complemented by using suitable constitutive relations and kinematic equations relating velocities to the rate of deformation tensors for both phases.

2.2.6 Some useful simplifications:

General model equations are composed of various variables, and in the case of saturated two-phase debris flow, they are made according to the following six variables:

- Volume fractions for the phases (n)

- Total stress (σ) and pore pressure (p_w)

- Velocities of the solid phase (v_s) and interstitial fluids (v_w)

The general model described above can be simplified in cases where

i. the gradient of porosity is small, and

ii. velocities of both phases are similar, i.e.

$$\frac{d^{(w)}}{dt} \approx \frac{d^{(s)}}{dt} = \frac{d}{dt} \tag{2.24}$$

which implies that the term $\frac{w^{\mathsf{T}}}{n}$.grad is small. the resulting model is written in terms of the following unknowns:

- Stress (σ) and pore pressure (p_w)

- Velocities of the mixture (v) and Darcy's velocity (ω)

If both balance of momentum equations are added, we obtain:

$$\rho \frac{dv}{dt} = \operatorname{div} \boldsymbol{\sigma}' - \operatorname{grad} p_w + \rho \mathbf{b} \tag{2.25}$$

where ρ is the mixture density and v the velocity of the solid skeleton.

The model is written in terms of v_s, v_w, $\boldsymbol{\sigma}'$, p_w and consists of the balance of mass of the mixture, balance of momentum of both the mixture and the fluid phase, and a suitable constitutive equation relating rate of deformation $d_s = \operatorname{grad}_{sym} v_s$ to the rate of stress tensors. The resulting model can be casted in terms of v, w and p_w, hence it is named $v_s - w - p_w$ Zienkiewicz-Shiomi model.

$$\begin{aligned}
\frac{1}{Q} \frac{d^{(w)} p_w}{dt} + \operatorname{div} \boldsymbol{w} + \operatorname{div} \boldsymbol{v}_s &= 0 \\
\rho \frac{dv}{dt} &= \operatorname{div} \boldsymbol{\sigma} + \rho \mathbf{b} = \operatorname{div} \boldsymbol{\sigma}' - \operatorname{grad} p_w + \rho \mathbf{b} \\
\rho_w \frac{dv_w}{dt} &= -\operatorname{grad} p_w + \rho_w \mathbf{b} - \mathbf{R}/n
\end{aligned} \tag{2.26}$$

In some cases [47, 45, 46], it can be assumed that the velocities and accelerations of the fluid phase in the pores are small with respect to the solid skeleton and accordingly, Darcy's velocity of the pore fluid can be eliminated. The resulting model is the widely used $\mathbf{u} - p_w$ or $\mathbf{v}_s - p_w$ Biot-Zienkiewicz model which is found in most geotechnical finite element codes used today.

2.2.7 Integration along depth

So far, we have considered three-dimensional continuum models which describe geomaterial flow in both the triggering and propagation phases. 3D formulations of mathematical models describing fast landslides are generally very computationally expensive. These models can be further simplified and reduced to a 2D formulation through depth integration approximation. Since many flow-like landslides have small average depths, or propagation heights, with respect to their length or width, the given equations can be integrated along the vertical axis. This results in an effective balance between accuracy and computational effort, making it suitable for modeling the majority of fast landslides.

We will use the reference system with axes $\{x_1, x_2, x_3\}$ sketched in figure 2.2. Z will denote the basal surface elevation, and h the depth of flowing mass. Velocities will be denoted as $\{v_1, v_2, v_3\}$, and sub-indexes s and w will refer to solid and fluid phases.
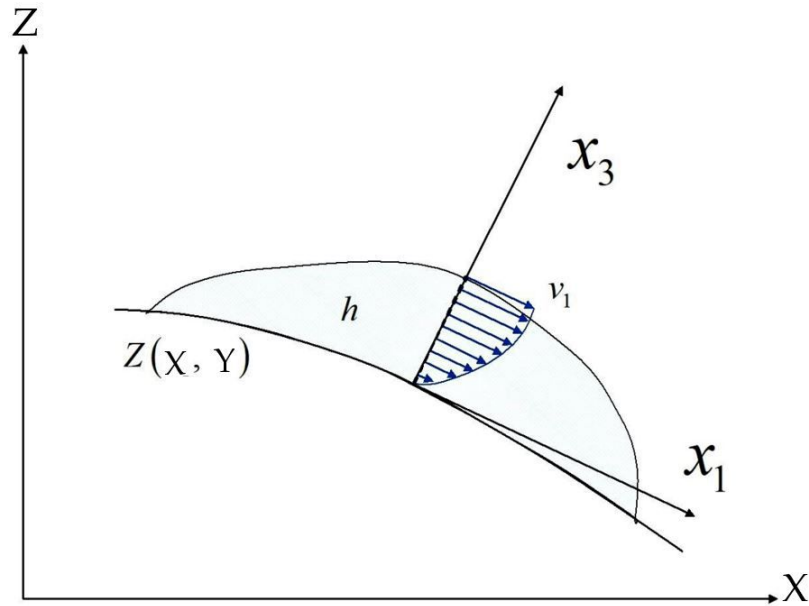

Figure 2.2: Reference system, coordinates and notation used in the analysis.

An overbar over a magnitude indicates it is a depth averaged value. For instance:

$$\bar{\theta} = \frac{1}{h} \int_0^h \theta \, dx_3 \tag{2.27}$$

Mixture averaged velocity ($\bar{v}$) is defined as follows:

$$\bar{v} = (1 - \bar{n})\bar{v}_s + \bar{n}\,\bar{v}_w \tag{2.28}$$

The "quasi material derivative" is expressed as:

$$\frac{\bar{d}}{dt} = \frac{\partial}{\partial t} + \bar{v}_j \frac{\partial}{\partial x_j} \quad j = 1, 2 \tag{2.29}$$

Based on Leibnitz's rule, depth integration is performed:

$$\int_a^b \frac{\partial}{\partial s} F(r, s)\,dr = \frac{\partial}{\partial s} \int_a^b F(r, s)\,dr - F(b, s)\frac{\partial b}{\partial s} + F(a, s)\frac{\partial a}{\partial s} \tag{2.30}$$

Our next step will be to introduce two auxiliary variables, h_s and h_w, which describe the contents of solids and fluids within a column of total height (h) (see Fig. 2.3).

$$\begin{aligned} h &= h_s + h_w \\ h_s &= (1 - n)\,h \quad h_w = nh \end{aligned} \tag{2.31}$$
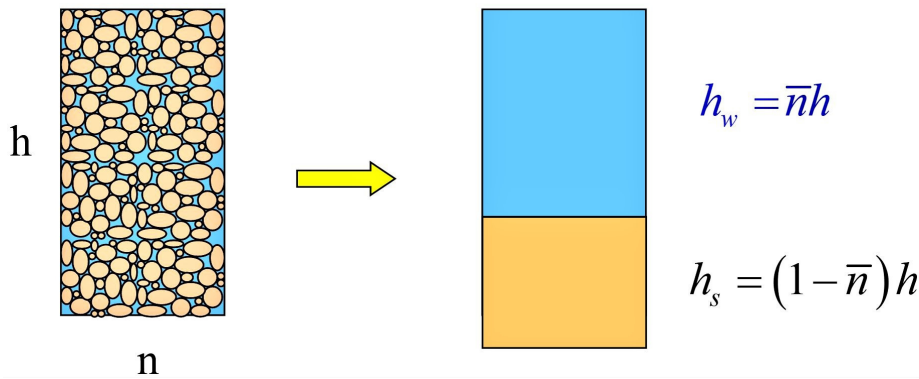

Figure 2.3: Definition of auxiliary variables h_s and h_w.

If we integrate the **balance of mass** equations along depth (local x_3 axis), we arrive at:

$$\begin{aligned} \frac{\bar{d}^{(s)}}{dt}\left((1 - \bar{n})\,h\right) + (1 - \bar{n})\,h\operatorname{div}\bar{v}_s &= (1 - \bar{n})\,e_R \\ \frac{\bar{d}^{(w)}}{dt}(\bar{n}\,h) + \bar{n}\,h\operatorname{div}\bar{v}_w &= \bar{n}\,e_R \end{aligned} \tag{2.32}$$

where e_R is the erosion rate, defined as the height increment of moving soil per unit time. There are various laws such as that proposed by Hungr et al. (2005)[16], which relate erosion rate to the depth averaged velocity of the flowing material.

After applying Leibnitz's rule to **balance of momentum equations** for both phases, we obtain:

$$
\rho_s h_s \frac{\bar{d}^{(s)}\bar{v}_s}{dt} = \text{div}\left(h\,\bar{\sigma}^{(s)}\right) - h\,\bar{p}_w\,\text{grad}\,\bar{n}
$$
$$
- \tau_b^{(s)} + \rho_s h_s \mathbf{b} + h_s\,\bar{\mathbf{R}}_s - (1-\bar{n})\,\rho_s\left(\bar{v}_s - \bar{v}_s^{(b)}\right)e_R
$$
$$
\rho_w h_w \frac{\bar{d}^{(w)}\bar{v}_w}{dt} = -\text{grad}\left(h\,\bar{p}_w\right) + h\,\bar{p}_w\text{grad}\,\bar{n}
$$
$$
- \tau_b^{(w)} + \rho_w h_w \mathbf{b} + h_w\,\bar{\mathbf{R}}_w - \bar{n}\,\rho_w\left(\bar{v}_w - \bar{v}_w^{(b)}\right)e_R \tag{2.33}
$$

where we have introduced the basal shear stresses of the solid and fluid phases as:

$$
\tau_{bi}^{(s)} = \left.-\sigma_{i3}^{(s)}\right|_Z \qquad \tau_{bi}^{(w)} = \left.-\sigma_{i3}^{(w)}\right|_Z \tag{2.34}
$$

The terms $\bar{v}_s^{(b)}$ and $\bar{v}_w^{(b)}$ denote the basal slip velocities of solid and water phases.

The depth averaged pore pressure ($\bar{p}_w$) will be decomposed into a hydrostatic part and an excess pore pressure as:

$$
\bar{p}_w = \bar{p}_{w,hydr} + \Delta\bar{p}_w \tag{2.35}
$$

One special case of particular interest is where the stresses in the solid phase are $\sigma_1 = \sigma_2 = \sigma_3$, the pore fluid being inviscid:

$$
\sigma_{ii} = ((1-n)\,\rho_s + n\rho_w)\,b_3\,(h - x_3) \quad i = 1..3
$$
$$
\sigma_{ii}^{(w)} = n\rho_w b_3\,(h - x_3) - n\,\Delta p_w \tag{2.36}
$$

from where we obtain:

$$
\sigma_{ii}^{(s)} = (1-n)\,\rho_s b_3\,(h - x_3) + n\Delta p_w \quad i=1..3
$$
$$
\sigma'_{ii} = (1-n)\,(\rho_s - \rho_w)\,b_3\,(h - x_3) + \Delta p_w \quad i=1..3 \tag{2.37}
$$

Then, the depth integrated equations are obtained as:

$$
\rho_s h_s \frac{\bar{d}^{(s)}\bar{v}_s}{dt} = \text{grad}\left\{\frac{1}{2}(1-\bar{n})\,\rho_s h^2 \mathbf{b}_3\right\} + \text{grad}\left(\bar{n}\,h\,\Delta\bar{p}_w\right)
$$
$$
+ \frac{1}{2}\rho_w h^2 \mathbf{b}_3\,\text{grad}\,\bar{n} - h\,\Delta\bar{p}_w\text{grad}\,\bar{n} \tag{2.38}
$$
$$
- \tau_b^{(s)} + \rho_s \mathbf{b} h_s + h_s\,\bar{\mathbf{R}}_s - (1-\bar{n})\,\rho_s\left(\bar{v}_s - \bar{v}_s^{(b)}\right)e_R
$$

for the solid phase, and

$$\rho_w h_w \frac{d^{(w)} v_w}{dt} = \operatorname{grad} \left\{ \frac{1}{2} \bar{n} \rho_w h^2 b_3 \right\} - \operatorname{grad} (h_w \Delta \bar{p}_w)$$

$$- \frac{1}{2} \rho_w h^2 b_3 \operatorname{grad} \bar{n} + h \Delta \bar{p}_w \operatorname{grad} \bar{n} \tag{2.39}$$

$$- \tau_b^{(w)} + \rho_w b h_w + h_w \bar{R}_w - \bar{n} \rho_w \left(\bar{v}_w - \bar{v}_w^{(b)} \right) e_R$$

for the fluid.

Above equations can be written in a more compact manner by introducing:

i. the pressure terms P_s and P_w defined as:

$$P_s = \left\{ -\frac{1}{2} (1 - \bar{n}) h^2 b_3 - \frac{1}{\rho_s} \bar{n} h \Delta \bar{p}_w \right\}$$

$$P_w = \left\{ -\frac{1}{2} \bar{n} h^2 b_3 + \frac{1}{\rho_w} \bar{n} h \Delta \bar{p}_w \right\} \tag{2.40}$$

ii. F_s and F_w:

$$F_s = \left\{ \frac{1}{2} \frac{\rho_w}{\rho_s} h^2 b_3 - h \frac{1}{\rho_s} \Delta \bar{p}_w \right\}$$

$$F_w = \left\{ \frac{1}{2} h^2 b_3 + h \frac{1}{\rho_w} \Delta \bar{p}_w \right\} \tag{2.41}$$

iii. and the source terms:

$$S_s = \frac{1}{\rho_s h_s} \left\{ \tau_b^{(s)} + \rho_s b h_s + h_s \bar{R}_s - (1 - \bar{n}) \rho_s \left(\bar{v}_s - v_s^b \right) e_R \right\}$$

$$S_w = \frac{1}{\rho_w h_w} \left\{ \tau_b^{(w)} + \rho_w b h_w + h_w \bar{R}_w - \bar{n} \rho_w \left(\bar{v}_w - v_w^b \right) e_R \right\} \tag{2.42}$$

The balance of momentum equations are now written as:

$$\frac{\bar{d}^{(s)} \bar{v}_s}{dt} = \frac{1}{h_s} \operatorname{grad} P_s + \frac{1}{h_s} F_s \operatorname{grad} \bar{n} + S_s$$

$$\frac{\bar{d}^{(w)} \bar{v}_w}{dt} = \frac{1}{h_w} \operatorname{grad} P_w + \frac{1}{h_w} F_w \operatorname{grad} \bar{n} + S_w \tag{2.43}$$

To simplify the notation, we will no longer use the overbar, assuming that all quantities are integrated over depth unless specified otherwise.

It is important to note that we have assumed $\sigma_1 = \sigma_2 = \sigma_3$ for solid phase. Equations 2.32, 2.38, and 2.39 govern the evolution of height (h), porosity (n), and the velocities of the solid and fluid.
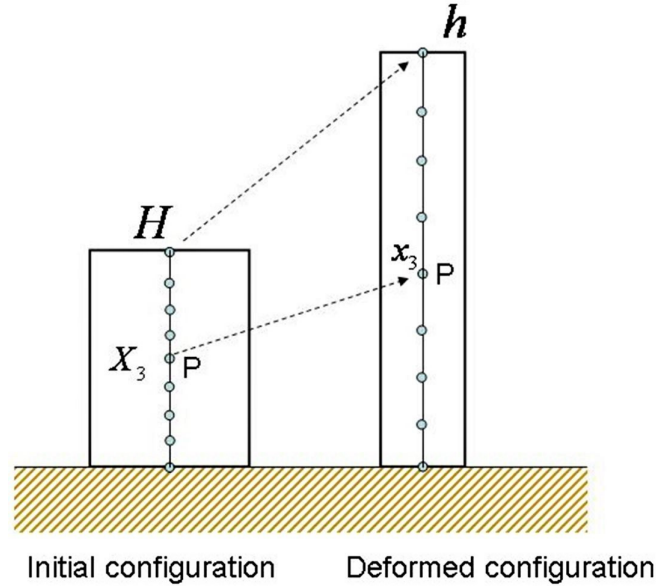
Figure 2.4: Deformation of a soil column.

2.2.8 Pore pressures

We will assume that the length and width of the mixture are significantly larger than its depth; therefore, the main dissipation mechanism will be vertical. However, changes in average porosity can induce corresponding changes in Δp_w.

Consider the soil column depicted in figure 2.4. On the left, the initial configuration is shown, and on the right, we see the deformed configuration. The column heights are denoted as H (initial) and h (deformed). The coordinates of both configurations are related as follows:

$$x_3 = X_3 \frac{h}{H} \tag{2.44}$$

In accordance with equation 2.33, the balance of momentum along x_3 can be expressed as:

$$n\rho_w \frac{d^{(w)} v_{w3}}{dt} = -n \frac{\partial p_w}{\partial x_3} + n\rho_w b_3 - \bar{C}_d w_3 \tag{2.45}$$

where the Darcy's velocity caused by vertical consolidation is indicated by w_3. According to equation 2.45, w_3 can be written as follows:

$$w_3 = -\frac{n}{\bar{C}_d} \frac{\partial p_w}{\partial x_3} + \frac{n}{\bar{C}_d} \rho_w b_3 - \rho_w \frac{n}{\bar{C}_d} \frac{d^{(w)} v_{w3}}{dt} \tag{2.46}$$

where we have introduced

$$\bar{C}_d = \frac{C_d}{n} \tag{2.47}$$

for convenience.

Based on the effective mean confining pressure and the pore-water pressure, we will define the mean confining pressure (p) as follows:

$$p = p' + p_w \tag{2.48}$$

From here, the material derivatives following the solid particles are:

$$\frac{d^{(s)}p_w}{dt} = \frac{d^{(s)}p}{dt} - \frac{d^{(s)}p'}{dt} \tag{2.49}$$

With regard to the term $\frac{d^{(s)}p}{dt}$, it corresponds to changes in height, while $\frac{d^{(s)}p'}{dt}$ can be derived using an appropriate constitutive equation for the soil skeleton. In fact, for elastic behavior, we can express it as:

$$\frac{d^{(s)}p'}{dt} = -\frac{K_v}{\alpha}\left(\frac{\partial v_{s3}}{\partial x_3} - d_{v0}\right) \tag{2.50}$$

where $K_v = \frac{E}{3(1-2v)}$ is the volumetric stiffness of soil skeleton, E the Young's modulus, v the Poisson's ratio, α being a constitutive parameter and d_{v0} describing additional dilatancy terms.

If the state of stress is such that $\sigma_1 = \sigma_2 = \sigma_3$, $\alpha = 1$, while under a state of stress $(k_0\sigma_1, k_0\sigma_1, \sigma_3)$, it is obtained $\alpha = k_0$.

The term $\frac{d^{(s)}p}{dt}$ is given by:

$$-\rho' b_3 \frac{d^{(s)}h}{dt}\left(1 - \frac{x_3}{h}\right) \tag{2.51}$$

where $\rho' = (1-n)(\rho_s - \rho_w)$.

Assuming $\sigma_1 = \sigma_2 = \sigma_3 = p$ we can obtain:

$$\frac{d^{(s)}p}{dt} = -\rho'b_3\left(\frac{d^{(s)}h}{dt} - \frac{d^{(s)}x_3}{dt}\right) = -\rho'b_3\frac{d^{(s)}h}{dt}\left(1 - \frac{x_3}{h}\right) \tag{2.52}$$

From equations 2.50 and 2.52, it follows:

$$\frac{d^{(s)}p_w}{dt} = -\rho'b_3\frac{d^{(s)}h}{dt}\left(1 - \frac{x_3}{h}\right) + \frac{K_v}{\alpha}\left(\frac{\partial v_{s3}}{\partial x_3} - d_{v0}\right) \tag{2.53}$$

Using the relations 2.14, we can approximate

$$\frac{\partial v_{s3}}{\partial x_3} = -\frac{\partial w_3}{\partial x_3} = \frac{\partial}{\partial x_3}\left(\frac{n}{\bar{C}_d}\frac{\partial p_w}{\partial x_3} - \frac{n}{\bar{C}_d}\rho_w b_3 + \rho_w\frac{n}{\bar{C}_d}\frac{d^{(w)}v_{w3}}{dt}\right) \tag{2.54}$$

The pore pressure term can be separated into two components: a hydrostatic ($p_{w,hyd}$) and an excess pore pressure (Δp_w). This can be expressed as:

$$p_w = p_{w,hyd} + \Delta p_w$$
$$\frac{\partial p_{w,hyd}}{\partial x_3} = \rho_w b_3$$

(2.55)

Taking into account the above equation, and neglecting the vertical acceleration along x_3, we obtain:

$$\frac{\partial v_{s3}}{\partial x_3} = \frac{\partial}{\partial x_3}\left(\frac{n}{\bar{C}_d}\frac{\partial \Delta p_w}{\partial x_3}\right)$$

(2.56)

The extra dilatancy is approximated as:

$$d_{v0} = \frac{1}{1-\bar{n}}\frac{d^{(s)}\bar{n}}{dt}$$

(2.57)

Therefore, we can conclude:

$$\frac{d^{(s)}\Delta p_w}{dt} = -\rho' b_3 \frac{d^{(s)}h}{dt}\left(1 - \frac{x_3}{h}\right)$$
$$+ \frac{K_v}{\alpha}\frac{\partial}{\partial x_3}\left(\frac{n}{\bar{C}_d}\frac{\partial \Delta p_w}{\partial x_3}\right) - \frac{K_v}{\alpha}\frac{1}{1-\bar{n}}\frac{d^{(s)}\bar{n}}{dt}$$

(2.58)

which is the equation describing the evolution of pore pressure. It comprises three terms:

i. The increment of excess pore pressure resulting from an increase in the height of the debris flow

ii. The consolidation along x_3

iii. The changes in average porosity as determined from the depth integrated equations.

2.2.9 Simplifications

Biot-Zienkiewicz-Shiomi h_s $h_w v_s$ $v_w - p_w$ and h $v - p_w$ simplified models can be obtained assuming porosity gradients are small. Then, the general equations are reduced to the following:

$$\rho_s h_s \frac{\bar{d}^{(s)}\bar{v}_s}{dt} = \text{grad}\left\{\frac{1}{2}(1-\bar{n})\rho_s h^2 b_3\right\} + \text{grad}\left(\bar{n} h \Delta\bar{p}_w\right)$$
$$- \tau_b^{(s)} + \rho_s b h_s + h_s \bar{R}_s - (1-\bar{n})\rho_s\left(\bar{v}_s - \bar{v}_s^{(b)}\right)e_R$$

(2.59)

for the solid phase, and

$$\rho_w h_w \frac{d^{(w)} \boldsymbol{v}_w}{dt} = \operatorname{grad} \left\{ \frac{1}{2} \bar{n} \rho_w h^2 b_3 \right\} - \operatorname{grad} \left(h_w \, \Delta \bar{p}_w \right)$$
$$- \, \boldsymbol{\tau}_b^{(w)} + \rho_w \boldsymbol{b} h_w + h_w \, \bar{\boldsymbol{R}}_w - \bar{n} \, \rho_w \left(\bar{\boldsymbol{v}}_w - \bar{\boldsymbol{v}}_w^{(b)} \right) e_R \tag{2.60}$$

for the fluid.

If we proceed with the assumption that:

$$\frac{\bar{d}^{(s)}}{dt} \approx \frac{\bar{d}^{(s)}}{dt} = \frac{\bar{d}}{dt} \tag{2.61}$$

we can add both momentum equations to obtain:

$$\rho h \frac{d\boldsymbol{v}}{dt} = \operatorname{grad} \left\{ \frac{1}{2} \rho h^2 b_3 \right\} - \boldsymbol{\tau}_b + \rho \boldsymbol{b} \, h - \rho \left(\bar{\boldsymbol{v}} - \bar{\boldsymbol{v}}^{(b)} \right) e_R \tag{2.62}$$

The balance of mass equation derives from the summation of the solid and fluid phases presented in equation 2.32, yielding the following result:

$$\frac{\bar{d} \, h}{dt} + h \operatorname{div} \bar{\boldsymbol{v}} = e_R \tag{2.63}$$

The pore pressure equation remains the same as equation 2.58, as obtained for the general case.

2.3 Numerical Methods

This section presents numerical methods used to discretize equations governing depth integrated mass and momentum conservation and excess pore pressure evolution. These methods are applicable in the propagation and consolidation stages of geotechnical studies. They help obtain approximate solutions when solving complex partial differential equations (PDEs) is not analytically feasible. The process involves transforming PDEs into ordinary differential equations (ODEs), making them suitable for particle-based simulation. This is accomplished through spatial and temporal discretization of the model.

Grid-based numerical methods such as the finite difference method (FDM) or the finite element method (FEM) have proven invaluable over the past decades, solving numerous scientific and engineering issues. However, in hydraulics and fluid mechanics, where large displacements are common, the use of meshes (especially with Lagrangian formulations) can lead to numerical difficulties. Meshless methods like SPH offer a compelling alternative, as they rely on moving points or nodes for discretization, thereby eliminating or minimizing the use of grids.

We briefly describe a Lagrangian meshless numerical method called Smoothed Particle Hydrodynamics (SPH) which is used to discretize the depth integrated equations presented. This method converts problems, originally in the form of partial differential

equations (PDEs), into formats suitable for particle-based simulation. SPH was first introduced by Lucy in 1977 and by Gingold and Monaghan (1977) to model astrophysical problems. Due to its ability to handle complex scenarios involving large displacements and deformations [19, 13], this technique has found applications in many areas, such as the modeling of rapid landslides in solid mechanics [20, 31, 37].

Considering this method, the purpose of this section is to describe a new model for problems where pore pressures play a significant role [34, 35].

2.3.1 Proposed SPH model

The depth-integrated mathematical model that we have selected to describe rapid landslides comprises a set of five equations. These equations address the balance of mass and momentum for both phases, as well as pore pressures. The variables include solid and fluid heights and velocities, which vary depending on position and time.

$$h_\alpha\left(x_1, x_2, t\right), \bar{v}_\alpha\left(x_1, x_2, t\right) \quad \alpha = s, w \tag{2.64}$$

The proposed method combines two sets of SPH nodes -for solid and water particles- with finite difference (FD) meshes associated to SPH nodes. The former sets describe the behaviour of depth integrated columns of soil and water, while the latter allows the analysis along depth of pore pressures. It is an improvement over models to implement pore pressures using simple approximations depending only on the value of the basal pore pressure.

We will introduce:

    i. two sets of nodes $\{x_{\alpha K}\}$ with $K = 1..N_\alpha$ where N_s and N_w are the number of SPH nodes in the solid and fluid phases, and,

    ii. the nodal variables:

        $h_{\alpha I}$ heights of phases at node I

        $\bar{v}_{\alpha I}$ depth averaged, 2D velocities

        and the pore-water pressure at the nodes $p_{wp\,I}$ which is a vector including the finite difference nodes along height.

In figure 2.5, we sketch the SPH soil and water nodes together with the finite difference meshes associated to each solid point to describe pore pressure evolution.
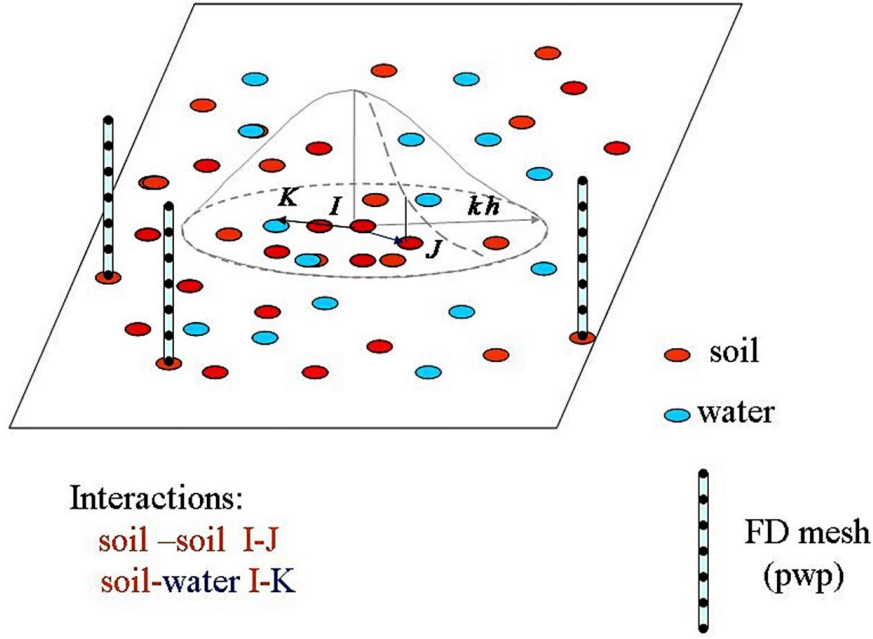
Figure 2.5: SPH nodes with FD meshes at solid nodes.

If the 2D area associated to a general fluid or solid node I is Ω_I, we will introduce for convenience, a fictitious volume m_I with dimensions L^3 moving with this node:

$$m_I = \Omega_I h_I \tag{2.65}$$

It is important to note that m_I has no physical meaning, as when node I moves, the material contained in a column of base Ω_I has entered it or will leave it as the column moves with an averaged velocity which is not the same for all particles in it.

Regarding the balance of mass equations, we have used a simple alternative, computing the heights from the position of the neighboring particles as:

$$[h_I] = \langle h(x_I) \rangle = \sum_J h_J \Omega_J W_{IJ} = \sum_J m_J W_{IJ} \tag{2.66}$$

The height can be normalized, which allows improving the approximation when SPH nodes are close to the boundaries:

$$h_I = \frac{\sum_J m_J W_{IJ}}{\sum_J \left(\frac{m_J}{h_J}\right) W_{IJ}} \tag{2.67}$$

We will recall here for convenience the momentum equations, writing them in a more compact form as:

$$\frac{\bar{d}^{(\alpha)} \bar{v}_\alpha}{dt} = \frac{1}{h_\alpha} \text{grad} \, P_\alpha + \frac{1}{h_\alpha} F_\alpha \, \text{grad} \, \bar{n} + S_\alpha \qquad \alpha = \{s, w\} \tag{2.68}$$

where the pressure terms are:

$$P_s = \left\{ -\frac{1}{2}\left(1 - \bar{n}\right)h^2 b_3 - \frac{1}{\rho_s}\bar{n}\,h\,\Delta\bar{p}_w \right\}$$

$$P_w = \left\{ -\frac{1}{2}\bar{n}\,h^2 b_3 + \frac{1}{\rho_w}\bar{n}\,h\,\Delta\bar{p}_w \right\}$$

(2.69)

and

$$F_s = \left\{ \frac{1}{2}\frac{\rho_w}{\rho_s}h^2 b_3 - h\frac{1}{\rho_s}\Delta\bar{p}_w \right\}$$

$$F_w = \left\{ \frac{1}{2}h^2 b_3 + h\frac{1}{\rho_w}\Delta\bar{p}_w \right\}$$

(2.70)

Finally, the source terms are:

$$S_s = \frac{1}{\rho_s h_s}\left\{ \tau_b^{(s)} + \rho_s b h_s + h_s \bar{R}_s - \left(1 - \bar{n}\right)\rho_s\left(\bar{v}_s - v_s^b\right)e_R \right\}$$

$$S_w = \frac{1}{\rho_w h_w}\left\{ \tau_b^{(w)} + \rho_w b h_w + h_w \bar{R}_w - \bar{n}\rho_w\left(\bar{v}_w - v_w^b\right)e_R \right\}$$

(2.71)

We will consider next how to discretize each of the three terms grad P_α, $\frac{1}{h_\alpha}F_\alpha$ grad $\bar{n}$ and S_α.

Regarding the gradient terms, we will write only one of the symmetrized forms, (see Monaghan 1982, 1985, 1992)[25, 24, 23]:

$$\frac{1}{h_{\alpha I}}\text{grad}\,P_{\alpha I} = -\sum_{1}^{N_{\alpha h}} m_J\left(\frac{P_{\alpha I}}{h_{\alpha I}^2} + \frac{P_{\alpha J}}{h_{\alpha J}^2}\right)$$

$$\frac{1}{h_{\alpha I}}\text{grad}\,\bar{n}_{\alpha I} = -\sum_{1}^{N_{\alpha h}} m_J\left(\frac{\bar{n}_{\alpha I}}{h_{\alpha I}^2} + \frac{\bar{n}_{\alpha J}}{h_{\alpha J}^2}\right)$$

(2.72)

which results on:

$$\frac{\bar{d}^{(\alpha)}}{dt}\bar{v}_{\alpha I} = \sum_J m_J\left(\frac{P_{\alpha I}}{h_I^2} + \frac{P_{\alpha J}}{h_J^2}\right)\text{grad}\,W_{IJ}$$

$$+ F_{\alpha I}\sum_J m_J\left(\frac{n_{\alpha I}}{h_I^2} + \frac{n_{\alpha J}}{h_J^2}\right)\text{grad}\,W_{IJ} + S_{\alpha I}$$

(2.73)

2.3.2 Pore pressure modeling

Excess Pore pressures with respect to hydrostatic can be written as:

$$\Delta p_w \left(x_1, x_2, x_3, t \right) \tag{2.74}$$

which is dependent on x_3 (vertical axis).

The consolidation expression given in equation (2.58) which is a classical parabolic partial differential equations is suitable for the formulation of FDM. Based on this, the second alternative numerical model was proposed by Pastor et al. (2015) [33], who combined a finite difference method (FDM) for the 1D equation of a vertical consolidation and depth-integrated SPH model for propagation analysis (SPH-FD model). Pastor et al. (2021) [35] extended this one-phase model to a two-phase model in order to fully approximate the pore pressures inside a landslide. In this technique, a finite-difference mesh, incorporated at each SPH node representing solid particles, is used to discretize pore–water pressures along the vertical axis, as depicted in figure 2.5.

Initial conditions describe the distribution of excess pore pressure across all FD meshes. We have assumed a simple linear law here, with values of zero at the top and $\Delta p_{wp,0}^{(b)}$ at the basal surface. The latter must be estimated either from field data or from the results of a model that describes the triggering of the landslide. These initial conditions play a pivotal role in the characteristics of debris flow propagation. When no data is available, an estimation is necessary.

As for boundary conditions, we have assumed a zero value at the top, while it is common to assume an impermeable boundary (zero flow) at the base. However, there are situations where the debris flow reaches mitigation structures such as basal screens, causing total pore pressure to dissipate and become equivalent to atmospheric pressure. This process causes the flow to slow down or even stop, as basal friction increases. Once the flow exits the screen, the flux returns to zero. In this context, our boundary conditions depend on the positions of the nodes on the terrain.

3 Rheological Model

3.1 Introduction

Thus far, various constitutive models have been introduced to consider the behavior of soil up to the point of failure. However, these models do not extend beyond this point due to their inability to accurately represent the propagation of fluidized material undergoing significant deformations. The aim of this section is to describe rheological models, which establish relationships between shear stress and the rate of shear strain. These models are utilized to study the propagation of the displaced mass. In this study, we will use simple shear infinite landslide models to calculate the basal shear stress (τ_B). This approach is more suitable for implementation in 2D depth-integrated models.

3.2 The simple shear flow

Simple shear infinite landslide models represent a particular case of simple-shear flows. In these models, (i) the flow is steady, and (ii) all magnitudes are independent of the position along the landslide, which is assumed to be of infinite length (fig. 3.1). This section is dedicated to presenting the infinite landslide model, and a method for calculating basal friction and depth-averaged stresses.
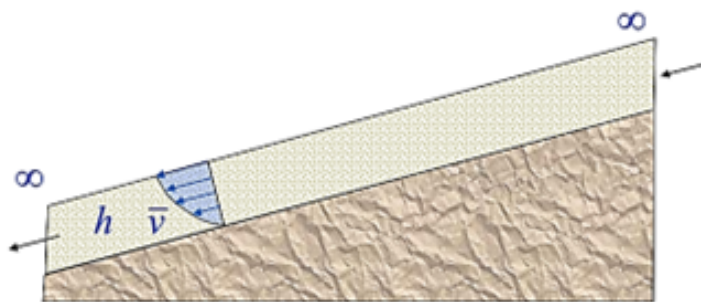

Figure 3.1: Simple shear infinite landslide

Our objective is to determine the basal forces per unit area and the depth integrated stresses without having information on the 3D flow structure, which is lost during the depth averaging process.
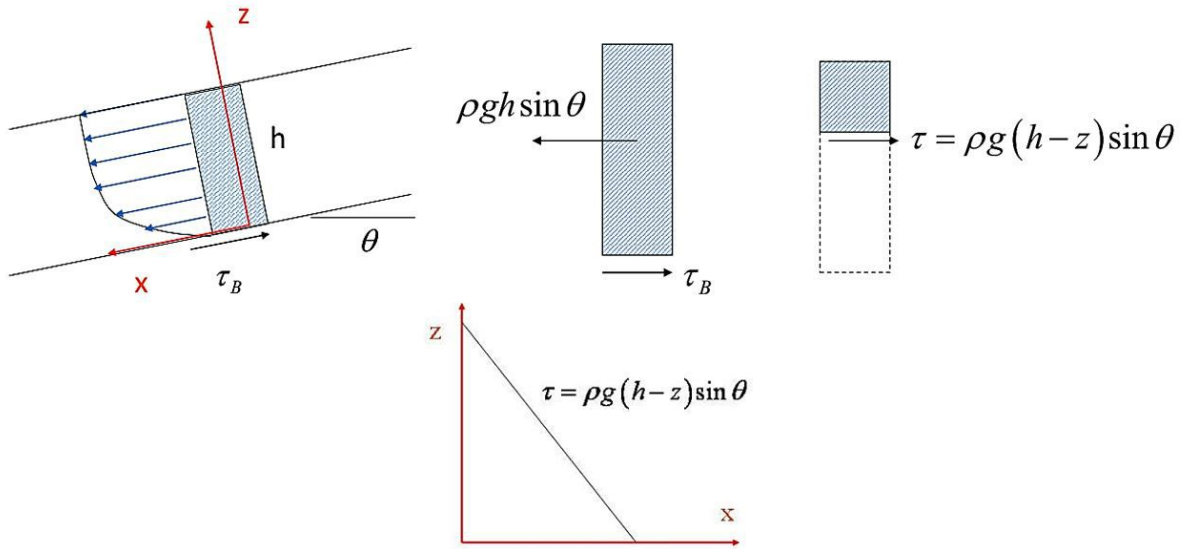
Figure 3.2: Simple shear infinite landslide diagrams

In the figure 3.2 a column of material of unit length and depth h is depicted. The flow structure is that of a simple shear flow. Since the acceleration along the x-axis is zero, the equilibrium of the column in figure 3.2 can be expressed as follows:

$$\rho g h \sin \theta = \tau_B \tag{3.1}$$

where ρ is the mixture density which has been defined in chapter 2, g the gravity acceleration, h the depth of flow, θ the slope angle, and τ_B the shear stress at the bottom. By considering the equilibrium of a part of the column extending from the surface to a depth $(h - z)$, we can obtain the shear stress as a function of z as:

$$\tau = \rho g (h - z) \sin \theta \tag{3.2}$$

Therefore, the shear stress varies linearly from zero at the surface to a maximum at the bottom, as given by equation 3.1. By substituting the basal shear stress provided in equation 3.1 into equation 3.2, the shear stress can then be obtained after eliminating the slope angle as follows:

$$\tau = \tau_B \left(1 - \frac{z}{h}\right) \tag{3.3}$$

The next step is to establish a relationship between the basal friction and the strain rate, which is formulated as:

$$\tau_B \left(1 - \frac{z}{h}\right) = f\left(\frac{\partial v}{\partial z}\right) \tag{3.4}$$

By integrating the previous expression, we obtain the velocity profile, $v(z)$. Subsequently, we can find the average depth integrated velocity, $\bar{v}$, and finally determine the

basal shear stress, τ_B, by rearranging the result. In the following sections, the most common rheological laws that relate shear stress to shear strain rate and are used in debris flow modeling will be introduced (fig. 3.3). Consider that the governing mathematical equations, given in chapter 2, include a basal friction term. Therefore, we will focus only on obtaining basal shear stress for the rheological models.
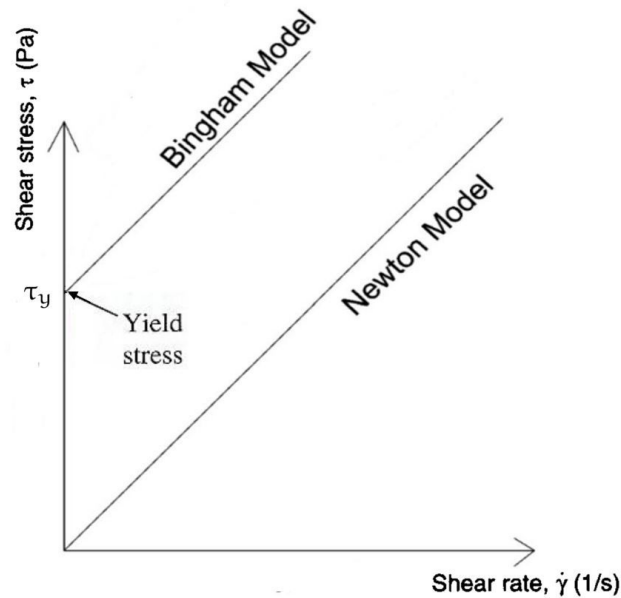

Figure 3.3: Rheological laws

3.3 Newtonian fluids

The Newtonian fluid is a simple rheological model characterized by one single constitutive parameter, the fluid viscosity. In the case of a simple shear flow, the shear stress is given by:

$$\tau = \mu \frac{\partial v}{\partial z} \tag{3.5}$$

where we have introduced the viscosity coefficient (μ) with units [Pa-s]. The last expression can be related to the shear stress equation 3.3 of the infinite landslide model as:

$$\mu \frac{\partial v}{\partial z} = \tau_B \left(1 - \frac{z}{h}\right) \tag{3.6}$$

Integrating the last expression along depth, the resulting velocity is obtained as:

$$v = \int \frac{\tau_B}{\mu} \left(1 - \frac{z}{h}\right) dz = \frac{\tau_B}{\mu} \left(z - \frac{z^2}{2h}\right) + c \tag{3.7}$$

where it is important to consider that the velocity is zero at the basal surface, $c = 0$. The depth integrated velocity can be related to the basal shear stress as:

$$\bar{v} = \frac{1}{h} \int_0^h v(z)\,dz = \frac{h\tau_B}{3\mu} \tag{3.8}$$

and therefore, the basal shear stress is obtained as:

$$\tau_B = \frac{3\mu\bar{v}}{h} \tag{3.9}$$

Consequently, one can conclude that an infinite slide in Newtonian fluids occurs when the slope is not zero and does not stop until the slope is zero.

3.4 Bingham fluids

The Bingham rheological model [4] is one of the simplest and most widely used viscoplastic models. It introduces a threshold shear stress that must be overcome to allow material flow and is able to explain phenomena such as formation of plug regions and stoppage of flows. In cohesive fluids, such as clay and water mixtures, flows exhibit yield stress. Their modeling was the pioneering work of Bingham (1922)[3]. In these models, the flow starts once the shear stresses exceed the threshold, represented by the yield stress (τ_y) then the movement is governed by a linear relationship between shear stress and strain rates, where the constant parameter of proportionality is called the coefficient of viscosity (μ). Rheological law governing Bingham fluid behavior is given by:

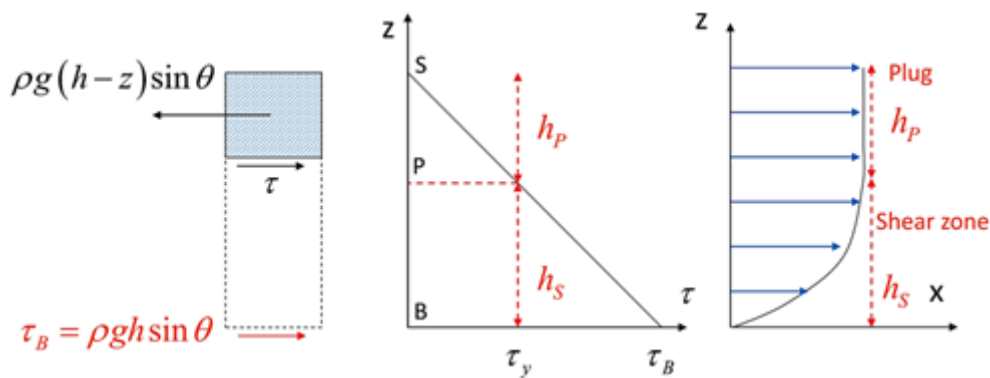$$\tau = \tau_y + \mu \frac{\partial v}{\partial z} \tag{3.10}$$

Figure 3.4: Flow structure of a Bingham fluid in an infinite simple shear flow.

Flow structure of a Bingham fluid, which is depicted in figure 3.4, consists of two separate parts:

i. From points S to P, which is called the "area of the plug", the mobilized shear stress is less than the yield stress. Considering that the velocity is constant in this region, therefore:

$$\frac{\partial v}{\partial z} = 0 \tag{3.11}$$

ii. From P to B, which is called the "cutting zone", the mobilized shear stress is greater than the yield stress and varies according to the following expression:

$$\frac{\partial v}{\partial z} = \frac{1}{\mu}\left(\tau_y - \tau\right) \tag{3.12}$$

Referring to figure 3.4, Some relations of interest are obtained as follows:

$$\begin{aligned} h_p &= \frac{\tau_y}{\rho g \sin\theta} = h\frac{\tau_y}{\tau_B} \\ h_s &= h\left(1 - \frac{\tau_y}{\tau_B}\right) \end{aligned} \tag{3.13}$$

Then, the relative plug height (η), which is a relation between the thickness of plug and total thickness, is defined as:

$$\eta = \frac{h_p}{h} = \left(1 - \frac{h_s}{h}\right) = \left(1 - \frac{\tau_y}{\tau_B}\right) \tag{3.14}$$

Likewise, by integrating over the depth, and calculating the average over the thickness, the following equation can be obtained:

$$\bar{v} = \frac{\tau_B h}{6\mu}(1 - \eta)^2(2 + \eta) \tag{3.15}$$

where η can be estimated by using the approximate method, proposed by Pastor et al. (2004)[32], which is based on using a polynomial economization technique.

3.5 Voellmy's law

It is a good alternative due to its simplicity and its ability to consider pore-water pressure at the basal surface. The basal shear stress of a pure frictional mass, ignoring cohesion and viscous terms, is given by:

$$\tau_B = \left(\rho'_d gh - \Delta p^b_w\right)\frac{\bar{v}_i}{|\bar{v}|}\tan\phi_B + \rho g\frac{|\bar{v}|}{\xi}\bar{v}_i \tag{3.16}$$

where h is the propagation height, ϕ_B the basal friction angle, $\bar{v}$ the depth averaged flow velocity, ξ the turbulence coefficient, and Δp^b_w the excess pore-water pressure at the basal surface, which is computed by using the consolidation equation 2.58. It can be seen in the above equation that the basal shear stress τ_B will depend on the basal excess

pore pressure, and it is modified in accordance with pore-water pressure's evolution at each node and time step [40]. Take into account that the higher the pore-water pressure, the lower the shear stress at the basal surface. In this study we disregard the additional turbulent term.

3.6 Sensitivity analysis

3.6.1 Introduction

Sensitivity analysis in geotechnical engineering plays a crucial role in improving the safety, effectiveness, and efficiency of engineering projects. The benefits of sensitivity analysis in this field include:

i. **Risk Assessment:** Sensitivity analysis helps in evaluating the risk and uncertainty associated with different aspects of geotechnical engineering. It can identify the factors or parameters that have a significant impact on the performance of an engineering system or project.

ii. **Decision Making:** It aids in decision-making processes by providing information on how changes in inputs impact the output. This allows engineers to make more informed decisions and prioritize areas of focus in the design process.

iii. **Design Optimization:** Sensitivity analysis is useful in optimizing designs by identifying which parameters most significantly affect performance. By understanding these relationships, it is possible to develop more effective and efficient designs.

iv. **Robustness of Models:** By understanding which parameters are most sensitive, engineers can ensure their models are robust against changes in these parameters. This is crucial for the reliability and validity of modeling in geotechnical engineering.

Overall, sensitivity analysis is a powerful tool in geotechnical engineering that enhances understanding, improves design, and mitigates potential risks. In this and the following chapters, we will perform several sensitivity analyses.

As a benchmark, we have chosen a 1D dam break problem to assess the factors affecting runout and propagation. It consists of the dam sketched in figure 3.5, with initial height equal to $10m$ and a length of $10m$. The dam is filled with a fluid with a density of $\rho = 1000\,Kg/m^3$. The fluid is contained by two walls, and at the time $0s$, the wall on the right is removed. This causes the fluid to flow along the horizontal plane. We established a checkpoint at $100m$ as a threshold for runout distance and recorded the relevant data at each time step.
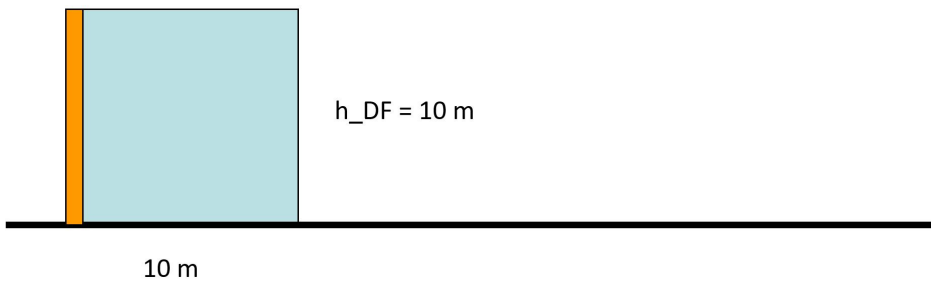
h_DF = 10 m

10 m

Figure 3.5: Initial configuration of the dam break problem.

When assessing the risk associated with landslides, two crucial factors can be considered:

1. **The time of propagation:** It refers to the duration from when a landslide is triggered to when it reaches its maximum extent. This can range from seconds in the case of rockfalls or debris flows, to weeks or even years for slow-moving landslides. A longer time of propagation allows more time for monitoring, warnings, evacuation, and implementation of mitigation measures.

2. **Impact force:** Landslides can destroy infrastructure and cause serious injury or even death to people in their path. It is determined by a variety of factors, including the height of the wave, mass, shape and angle of Impact, and speed.

3.6.2 Influence of viscosity

Viscosity, in fluid dynamics, is a measure of a fluid's resistance to shear or flow. In general, higher viscosity leads to slower flow rates. This is because the fluid resistance is higher, making it more difficult for the fluid to move. Figure 3.6 shows the displacement-time graph in the case of a Newtonian fluid with different viscosities.
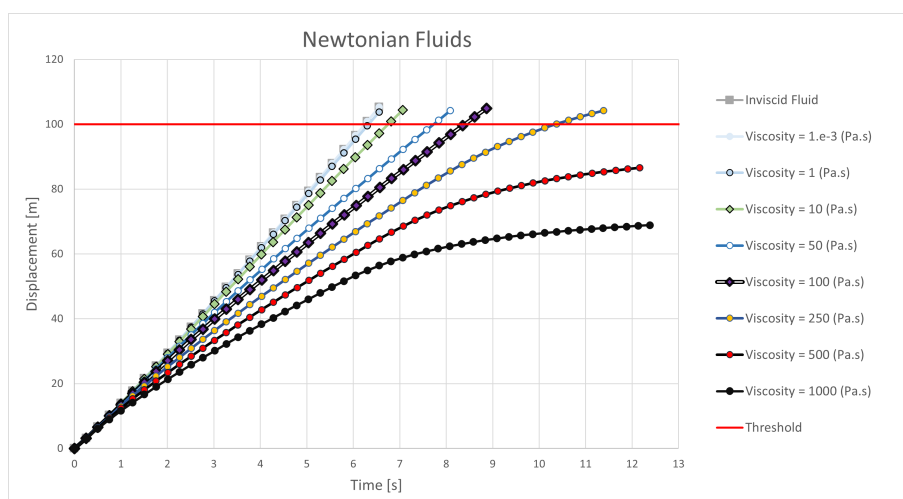

Figure 3.6: Displacement-time graph for Newtonian fluids

Furthermore, figure 3.7 displays the velocity-time graph for a Newtonian fluid with different viscosities. As evident, even a highly viscous fluid will not stop flowing; however, they will reach small velocities.
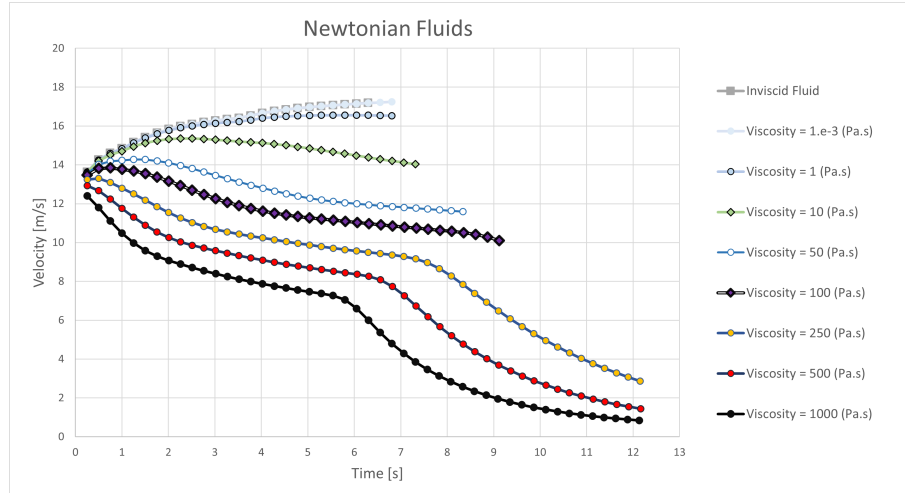

Figure 3.7: Velocity-time graph for Newtonian fluids

The longitudinal profiles of the flows are illustrated in figure 3.8. A higher viscosity fluid would generally develop a thicker layer and is more likely to experience a laminar (smooth and orderly) flow.
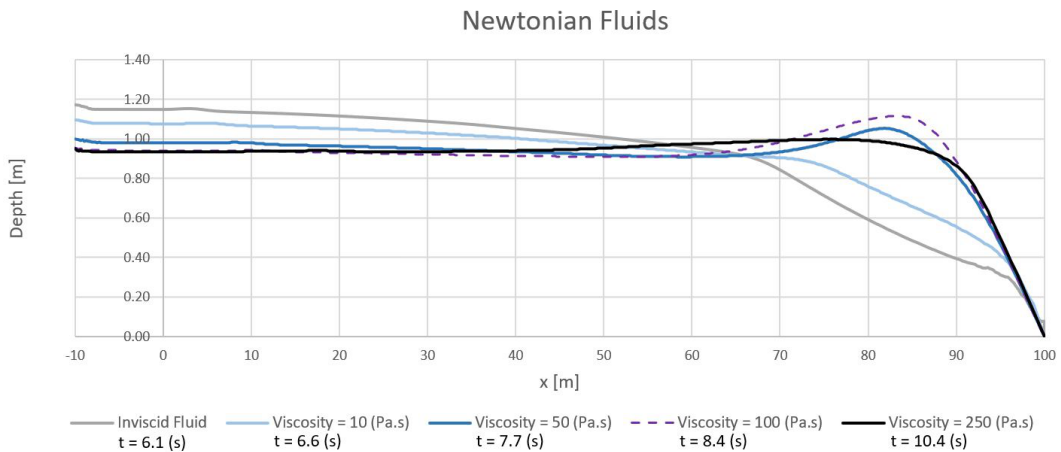

Figure 3.8: Longitudinal profiles and corresponding arrival times for Newtonian fluids

It can be concluded that, for this problem, Newtonian fluids with viscosities lower than 250 (Pa.s) could potentially cause damage at our checkpoint, since the propagation time of these fluids is low and they maintain their velocity throughout their path.

3.6.3 Influence of yield stress

In viscoplastic fluid dynamics, yield stress is a fundamental parameter that greatly influences how the fluid propagates, deforms, or resists deformation under different conditions. As mentioned before, viscoplastic fluids like Bingham fluids tend to form a plug zone in the upper region where the fluid behaves more like a solid because the stress is lower than the yield stress. In order to make a parametrical analysis, we fixed the viscosity at 100 (Pa.s) and gradually increased the yield stress. Figure 3.9 illustrates the result for displacements as a function of time.
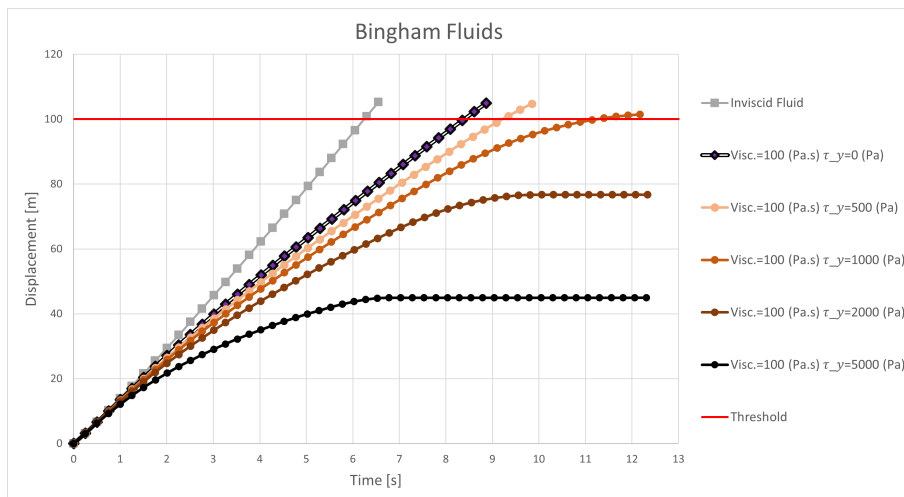

Figure 3.9: Displacement-time graph for Bingham fluids

Additionally, the velocity-time graph for different yield stresses is shown in figure 3.10. It is imperative to notice that viscoplastic fluids stop flowing when driving stresses become lower than yield stresses.
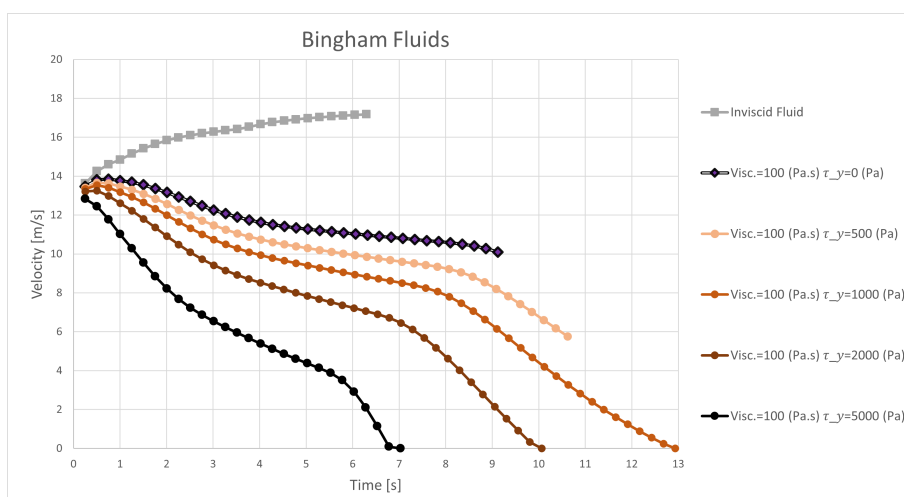

Figure 3.10: Velocity-time graph for Bingham fluids

Finally the longitudinal profiles of the flows are depicted in figure 3.11. The size of the plug zone is influenced by the yield stress - higher yield stresses typically result in larger plug zones, thus a steeper slope in the front region of the flow.
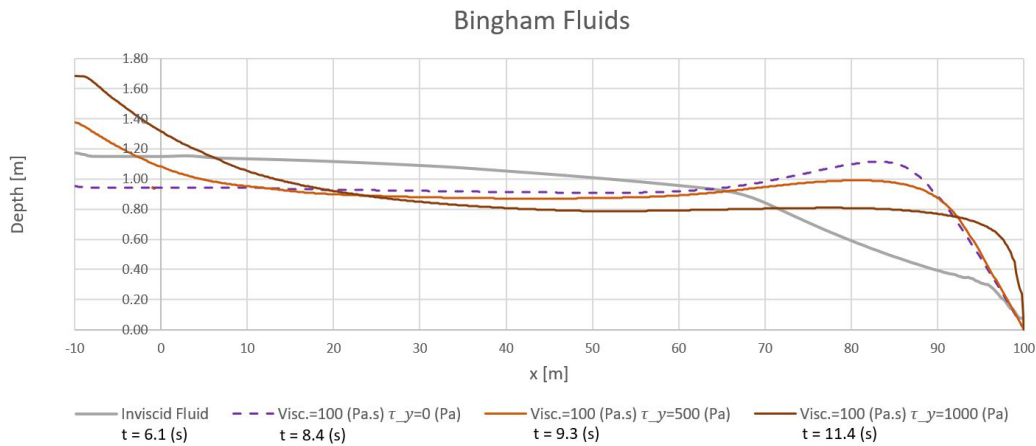

Figure 3.11: Longitudinal profiles and corresponding arrival times for Bingham fluids

These results indicate that yield stress can determine the flow profile shape. It can also be observed that a fluid with a yield stress exceeding 1 (kPa) has no impact on our control point.

3.6.4 Influence of friction angle

Voellmy's law, uses Coulomb friction angle to estimate shear resistance. Lower friction angles can result in landslides moving faster and farther because the resisting forces are smaller. On the other hand, a higher friction angle can slow the movement and reduce the distance the landslide travels because of increased resistance to motion. Figure 3.12 shows the displacement-time graph for different friction angles.
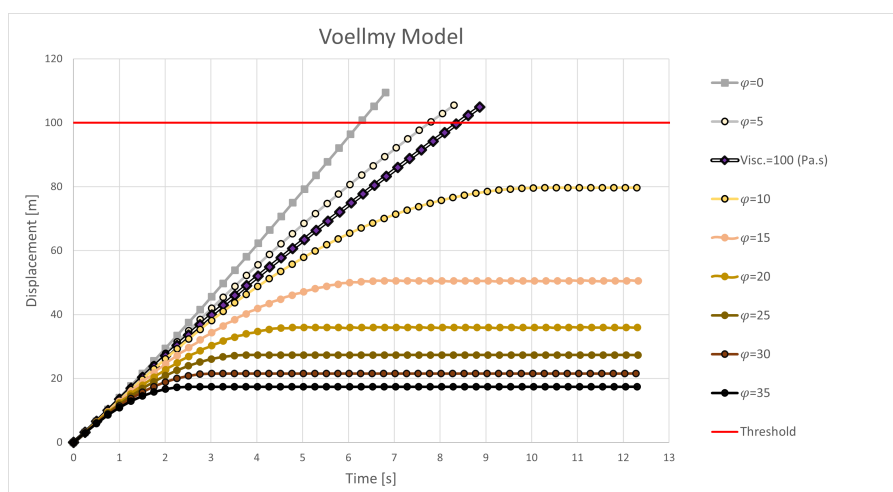

Figure 3.12: Displacement-time graph for Voellmy model

When the slope angle (the angle the deformed material makes with the horizontal) is less than the friction angle, then the material will stop flowing, i.e. the velocity reaches zero. The velocity-time graph for different friction angles is demonstrated in figure 3.13.
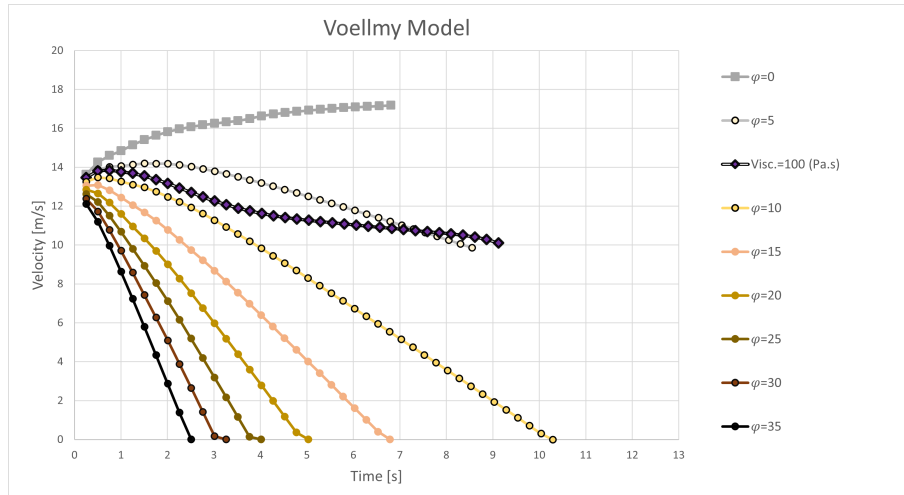
Figure 3.13: Velocity-time graph for Voellmy model

In figure 3.14, we can see the longitudinal profiles of the flows. A higher friction angle might lead to a more stable post-landslide slope, while a lower one may increase the likelihood of subsequent failures.

Figure 3.14: Longitudinal profiles and corresponding arrival times for Voellmy model

All things considered, for friction angles larger than 10°, the material flow will not reach and therefore pose any risk to our checkpoint.

4 Two-Phase Model

4.1 Introduction

As mentioned in the previous chapters, the debris flow propagation stage is greatly influenced by the time-space evolution of the pore-water pressure. As a result, two-phase modeling is crucial to consider pore pressure variations and precisely simulate debris flows' complex behavior. In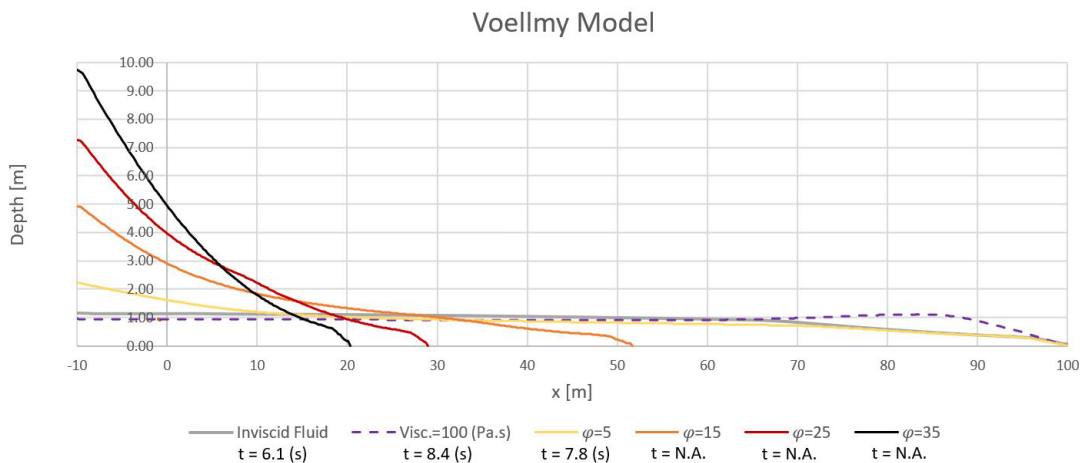 this chapter, we will first describe the phenomenon of dewatering. Then, we will introduce the similar one-dimensional dam break problem as a benchmark and compare the simulation results of our general model with the simpler approximations which do not consider excess pore pressure. Moreover, we will discuss the impact of solid phase elastic modulus on consolidation rate and runout distance. Also a comparison will be made between a high permeable soil and a low permeable one. Lastly, basal screens will be proposed as a mitigation structure to reduce debris flow velocity and run out distance. It is interesting to note that the selected countermeasure involves pore-water pressure dissipation. Thus, the modeling framework should capture this debris flow phenomenon.

4.2 Dewatering

To extend the proposed model to the most general case, we consider the case of the partially saturated soil, which consists of three components: a mixture consisting of soil grains, water, and air. We need to adjust propagation models to capture unsaturated soil's dynamic behavior and mechanisms. Therefore, it is essential to consider another material layer for the air phase.

Figure 4.1-a shows a simplification of reality, where a saturated layer exists at the bottom, where α is the relative height and αh the depth of the saturated zone, and there is a top layer of unsaturated soil. In this model, a degree of saturation (S_r) is considered only for the top layer. Therefore, in this study, we have considered a general case where the total height h is divided into three layers, as shown in Figure 4.1-b. The partial heights of solid, fluid, and air can be obtained, respectively, as follows:

$$h_s = (1 - \bar{n})\, h \tag{4.1}$$

$$h_w = \bar{n}\, (\alpha + S_r\, (1 - \alpha))\, h \tag{4.2}$$

$$h_a = \bar{n}\, (1 - S_r)\, (1 - \alpha)\, h \tag{4.3}$$

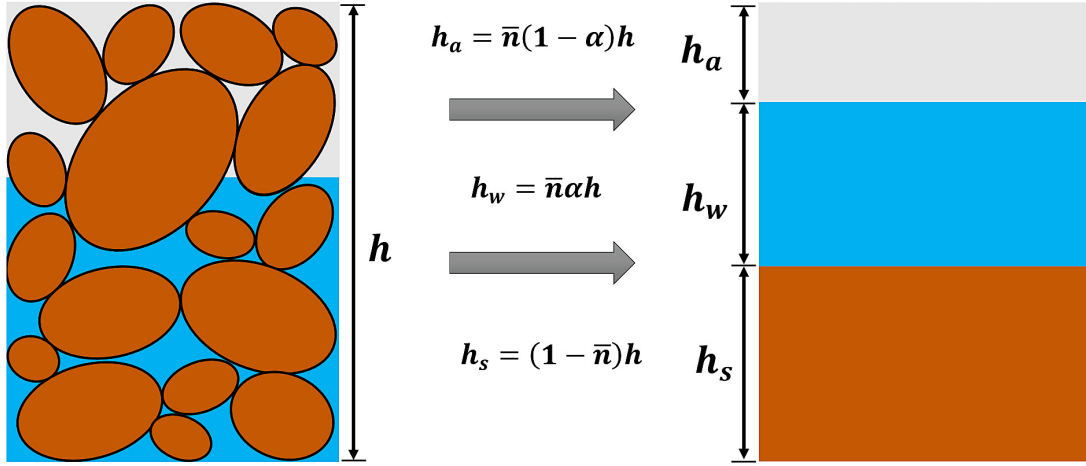where $\bar{n}$ is the averaged porosity.

Figure 4.1: Magnitudes characterizing the partially saturated debris flow components

What happens is that once the porosity reaches a lower bound $\bar{n}_{min}$ (which depends on the solid grains' size distribution), the upper part of the sliding mass will be unsaturated. During the computations, we obtain h_w and h_s from the balance of mass equations; the porosity is computed as:

$$\bar{n} = \frac{h_w}{h_s + h_w} \geqslant \bar{n}_{min} \qquad (4.4)$$

If at a certain time it reaches the limit, we will compute the depth of the saturated layer as:

$$\alpha = \frac{1}{1 - S_r} \left(\frac{1 - \bar{n}_{inf}}{\bar{n}_{inf}} \frac{h_w}{h_s} - S_r \right) \qquad (4.5)$$

where $\bar{n}^{n+1} = \left(h_w^{n+1} / h^{n+1} \right) \leqslant \bar{n}_{inf}$.

If we are given h_s, h_w, S_r and α, the total height can be obtained as:

$$h = \frac{h_s + h_w}{[1 - \bar{n}\,(1 - S_r)\,(1 - \alpha)]} \qquad (4.6)$$

This remarkable phenomenon is called dewatering. In the paper published by Tayyebi et al.[40], the altered balance equations of mass and linear momentum for partially saturated soils have been proposed. As shown in Figure 4.2, a two-layer model is presented. The hydrostatic and excess pore-water pressures are considered for the lower layer. A null pore-water pressure value is assumed at the layer above the water table.
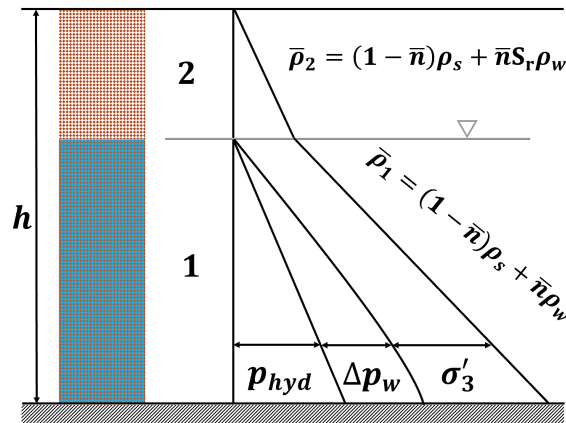
Figure 4.2: Pore-water pressure distribution in solid-fluid mixture of total height h. The lower layer (Layer 1) is fully saturated, whereas the upper layer (Layer 2) could be partially saturated or dry ($S_r = 0$).

4.3 A dam break problem

Like before, we have chosen a 1D dam break problem as a benchmark. It consists of the dam sketched in Fig. 4.3, with a initial height of the material equal to 10m. and a length of 10m.

Figure 4.3: Initial configuration of the dam break problem.

The dam is filled with a saturated loose granular material with densities of solid particles and fluid $\rho_s = 2400 \, \text{Kg/m}^3$ $\rho_w = 1000 \, \text{Kg/m}^3$ and an initial porosity of 0.42, for which the mixture density is $\rho = 1800 \, \text{Kg/m}^3$. The minimum porosity ($n_{min}$) of the material is assumed to be 0.4.

The material is contained by two walls, and at time 0s, the wall on the right is removed, which causes the material to liquefy. Then, the debris flow propagates along the horizontal plane.

To assess the factors upon which runout and propagation depend, we have made several parametrical analysis. This would give us a better insight into the multifaceted problem of debris flow propagation.

4.4 Influence of pore-water pressure

To emphasize on the influence of the pore-water pressure on the runout distance for the two-phase debris flow model, a comparison is made between the added pore-water pressure extension or without it (fig. 4.4).
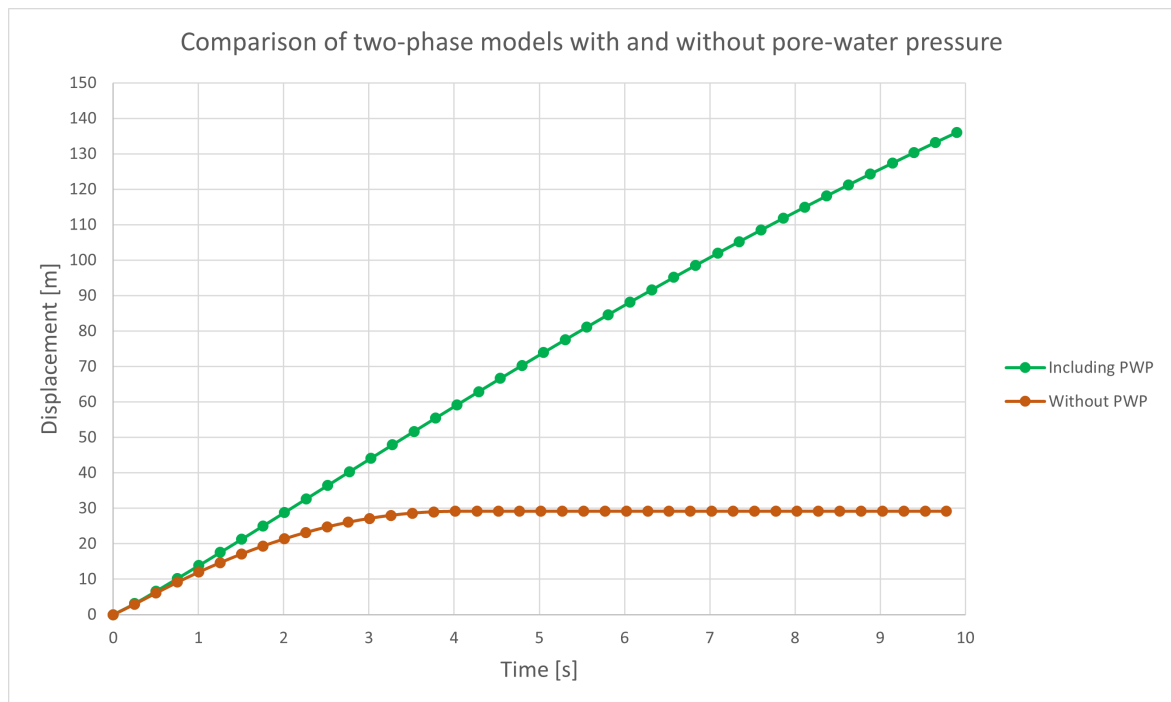
Figure 4.4: Comparison of the runouts of two-phase debris flow models with and without pore-water pressure

As evident, pore-water pressure influences propagation in a profound manner, causing a larger runout distance and a higher velocity, especially in cases where consolidation occurs slowly such as materials with low to medium permeability.

4.5 Influence of elastic modulus

According to equation 2.58, the vertical consolidation rate (second term) is proportional to the volumetric stiffness of the soil skeleton, which in turn depends on the soil's Young's modulus. Therefore, it is interesting to investigate the effect of elastic modulus on runout distance, as a larger runout indicates a slower consolidation rate.
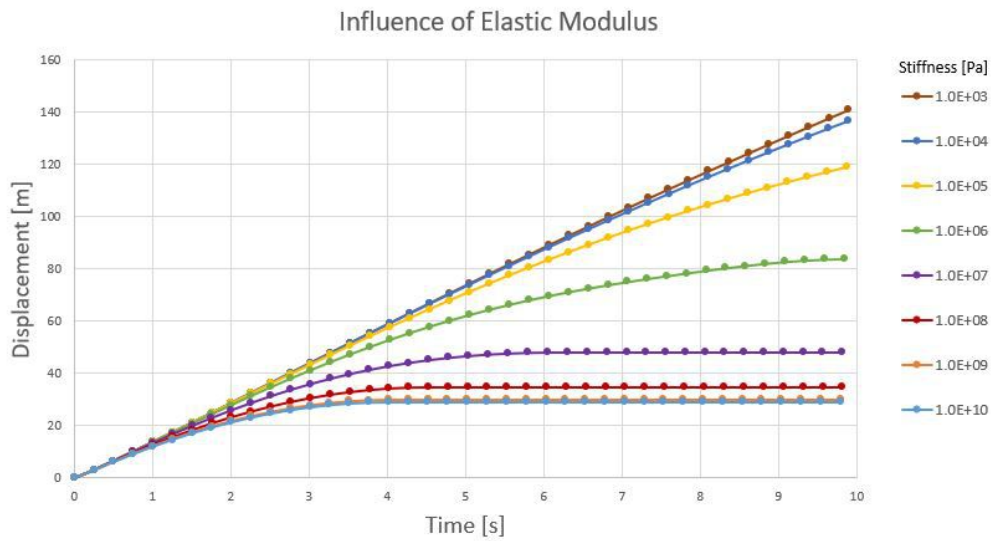
Figure 4.5: Impact of the elastic modulus on the runout distance

4.6 Influence of permeability

In section 2.2.5 some interaction laws have been introduced. Here we will use Anderson and Jackson law[1] where terminal velocity will be used as a measure of permeability. To assess the effect of permeability on runout distance, a comparison will be made between high and low permeable soil with the corresponding terminal velocity (V_T) equal to $1^m/_s$ and $10^{-5} {}^m/_s$, respectively.

Figure 4.6: Impact of the permeability on the runout distance

It is important to mention that, since high permeable saturated soil undergoes consolidation rapidly, pore fluid abandons the solid skeleton and has a larger displacement.

4.7 Basal Screens

A basal screen is a structure constructed at the base of a slope or hillside to reduce the runout distance of landslides. The purpose of the basal screen is to intercep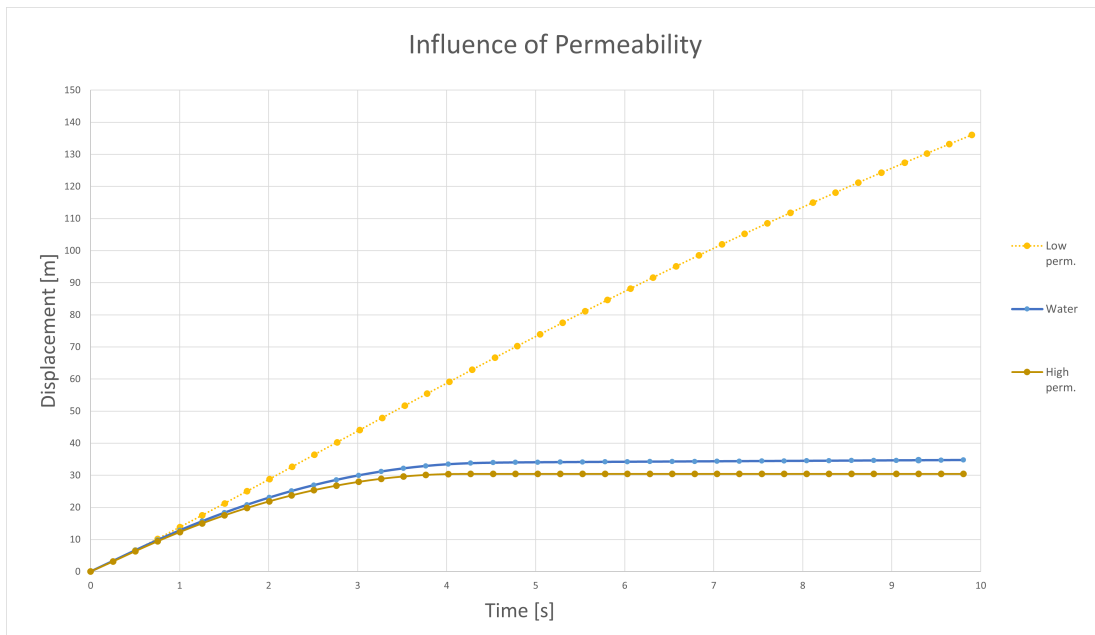t and contain the mass of soil or rock material that is moving downslope during a landslide event. These structures usually consist of parallel steel rods, with a specified gap between them, built on a horizontal flat-deck structure (fig. 4.7). It also has a simple structural design and can be easily installed, repaired, and maintained.
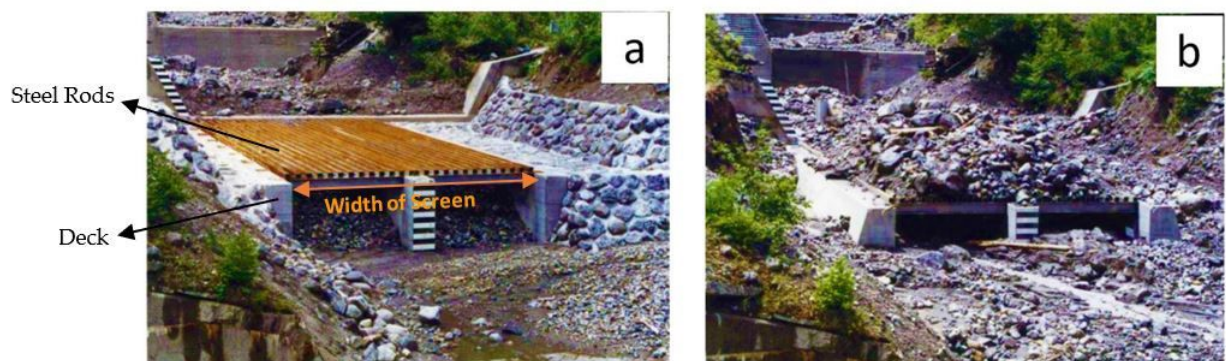

Figure 4.7: Bottom drainage screens in the Kamikami-Horisawa Valley, (a) before and (b) after the occurrence of a debris flow [14].

The idea of installing bottom drainage screens along the propagation path of debris flows to reduce their impact was proposed by Hashimoto in Japan in the 1950s [14]. Due to the effectiveness of this energy dissipating structure, several small-scale physical models have been conducted to have a better understanding of debris-flow screens and their mechanism including:

 i. The effects of different opening widths of permeable screens on the debris-flow run-out distance [14].

 ii. The effects of different bed sediments with different blocking and opening widths [18].

 iii. The effects of different locations of debris flow screens, in the middle or at the end of the propagation path, on the behaviour of debris flows [43].

When the flowing mass propagates over the screen, some water outflows through the basal screen. Thus the degree of saturation of debris flow is reduced and dewatering occurs. In order to study this effect, we have chosen a single node located in the middle

of the reservoir. The basal pore pressure was monitored over time both without and with screens (fig. 4.8).
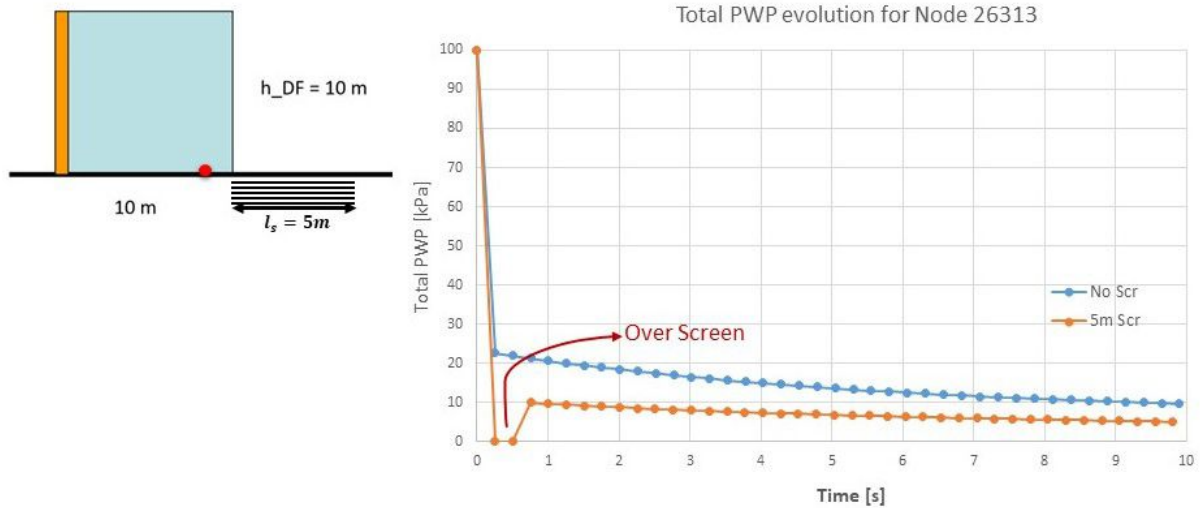

Figure 4.8: Influence of screen on total pore pressure

Analyzing both curves, we can observe a sudden drop in total pore pressure. This is due to the combined effect of consolidation and a decrease in the height of the mixture column corresponding to the node. Moreover, it is evident that when the node travels over the drainage screen, the basal pore-water pressure is fully dissipated.

During the runout, the total pore-water pressure (p^b_{tot}) is a sum of the hydrostatic (p^b_{hyd}) and the excess pore-water pressure (Δp^b_w). When the moving mass runs over a permeable screen, the total pore-water pressure (p^b_{tot}) at the basal surface becomes zero. Consequently, at the basal surface, the hydrostatic pressure (p^b_{hyd}) instantly becomes equal, but opposite in sign, to the excess pore-water pressure (Δp^b_w). Therefore, negative values of excess pore-water pressure (Δp^b_w) is expected over the permeable screen.

4.8 Influence of screen on different permeabilities

In this section, some parametrical analyses will be done to identify which factors most significantly affect the performance of permeable screens. By understanding these aspects, it is possible to develop more effective and efficient designs.

Figure 4.9 demonstrates the runouts for high permeable soil ($V_T = 1^m/_s$) and low permeable soil ($V_T = 10^{-5}\ ^m/_s$) as well as displacements in the presence of basal screens of different lengths.
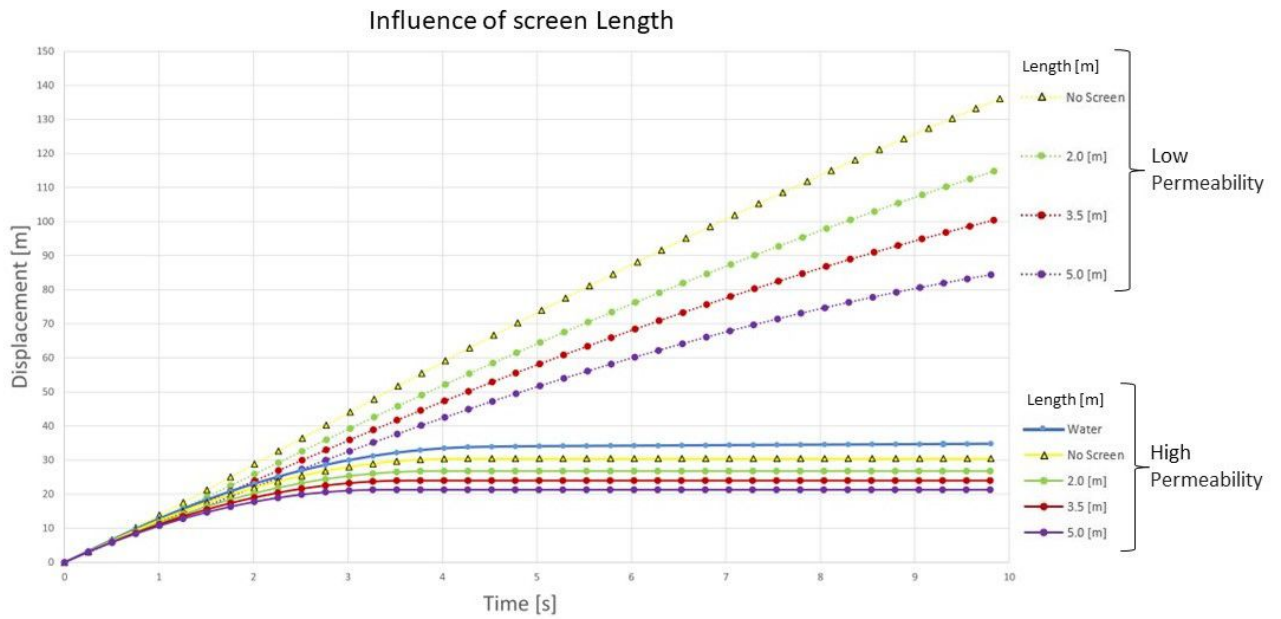
Figure 4.9: Influence of screen on runout distance

Moreover, to better comprehend the efficacy of screens on decreasing runout distance, the displacements (at t = 10s) as a function of screen length are depicted in figure 4.10.
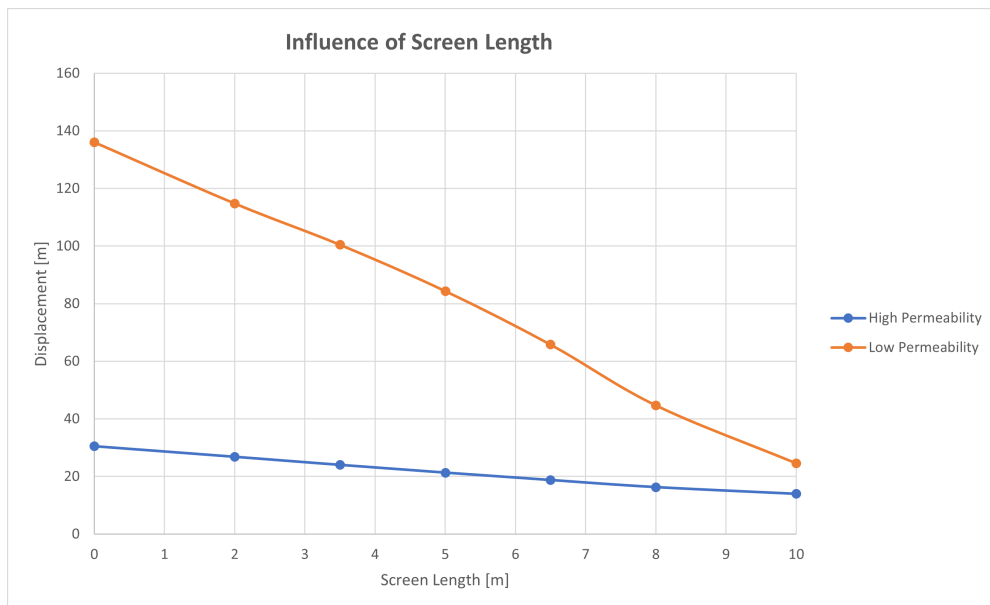
Figure 4.10: Influence of screen on different permeabilities

According to figure 4.10, for low permeable soil, runout distance decreases sharply with a longer screen. Thus, this structural countermeasure is most effective for low permeabilities. Figure 4.11 illustrates the profiles of the mixture as it flows on the horizontal plane and its corresponding porosities for both high (a) and low (b) permeabilities.
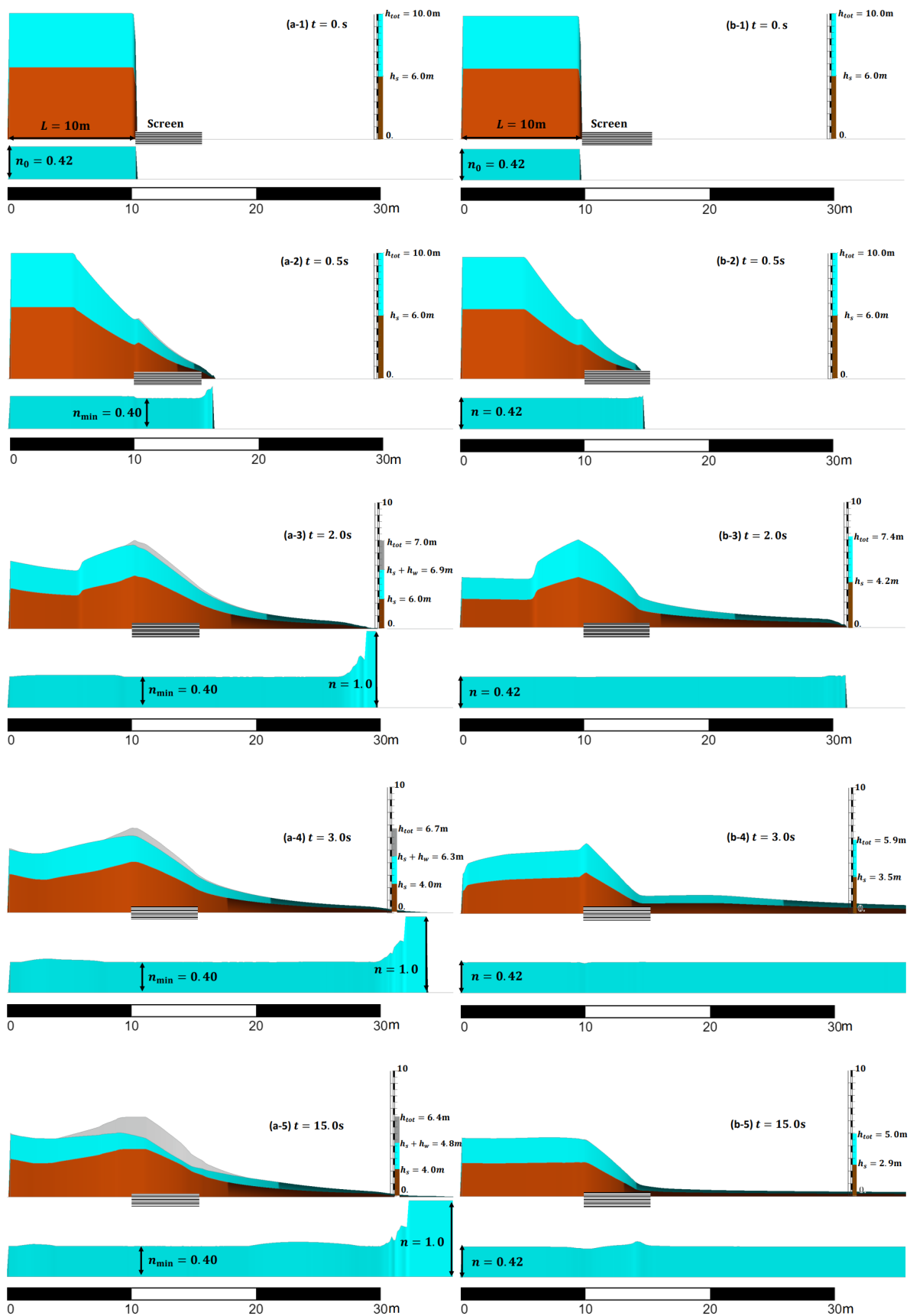
Figure 4.11: The profiles of the propagation heights and their corresponding porosity of dam break problems with (a) high and (b) low soil permeability.

As evident in figure 4.11(a), for higher soil permeability, the dewatering rate is greater. This changes the dynamic behavior of the propagation mass. As shown in figure 4.11(a-2:5), for high permeable soil on the basal screen, the minimum porosity of the material (in this case 0.4) is reached, and desaturation starts. Dewatering of soil reduces the fluid volume fraction in the upper part of debris flow. Consequently, the upper part of the propagation mass may become dry, but the lower part remains fully saturated. These factors lead to a hill-shaped accumulation over the screen (fig. 4.11 (a-2:5)).

It is also interesting to note that for high permeable soil, after a certain time (fig. 4.11 (a-3:5)), on the front side of the propagation mass, separation between the fluid and solid phases occurs. Causing the fluid to travel at higher ranges and the porosity to equal 1.

As shown in figure 4.11(b-2:5), in the dam break problem with low permeable soil, the desaturation rate is low, and the porosity remains constant. This indicates that the low permeability of the soil minimizes water outflow from the soil, and the propagation mass maintains its mobility.

As mentioned previously, bottom drainage screens are designed to dissipate basal pore-water pressure and desaturate flowing mass. In figure 4.12, we provide the distribution of excess pore-water pressure at different time steps corresponding to debris flows consisting of high (fig. 4.12(a)) and low (fig. 4.12(b)) soil permeability.

As shown in figure 4.12(a-1,b-1), the excess pore-water pressure at the base (Δp_w^b) is equal to 100 kPa which is approximately equivalent to 10 meters of water column. This indicates that the flowing material is completely liquefied when the dam on the right side collapses. It can be seen in figure 4.12 that once the moving mass passes over the permeable screen, the basal total pore-water pressures (p_{tot}^b) of the debris flows become equal to the atmospheric pressure and the basal excess pore-water pressures (Δp_w^b) become negative.

Furthermore, it is crucial to keep in mind that in depth-integrated models, the vertical axis of magnitudes, such as pore-water pressure, is eliminated. Therefore, it is necessary to implement an additional consolidation equation describing how pore pressure evolves over time and depth. One of the advantages of the SPH-FD model is the ability to simulate cases where basal pore pressures drop to zero due to a landslide crossing a terrain with very high permeability.

In addition to that, due to the dissipation of pore-water pressures through the basal screens, soil particles regain their contact friction. Therefore, the basal shear stress of the flowing material increases, which the presented model is capable of considering it using the Voellmy rheological equation.

As a comparison between the cases of high (fig. 4.12(a)) and low (fig. 4.12(b)) soil permeability, one can observe that drainage screens affect a larger domain in a permeable environment. While for a low permeable soil, the impact is almost limited to the base.
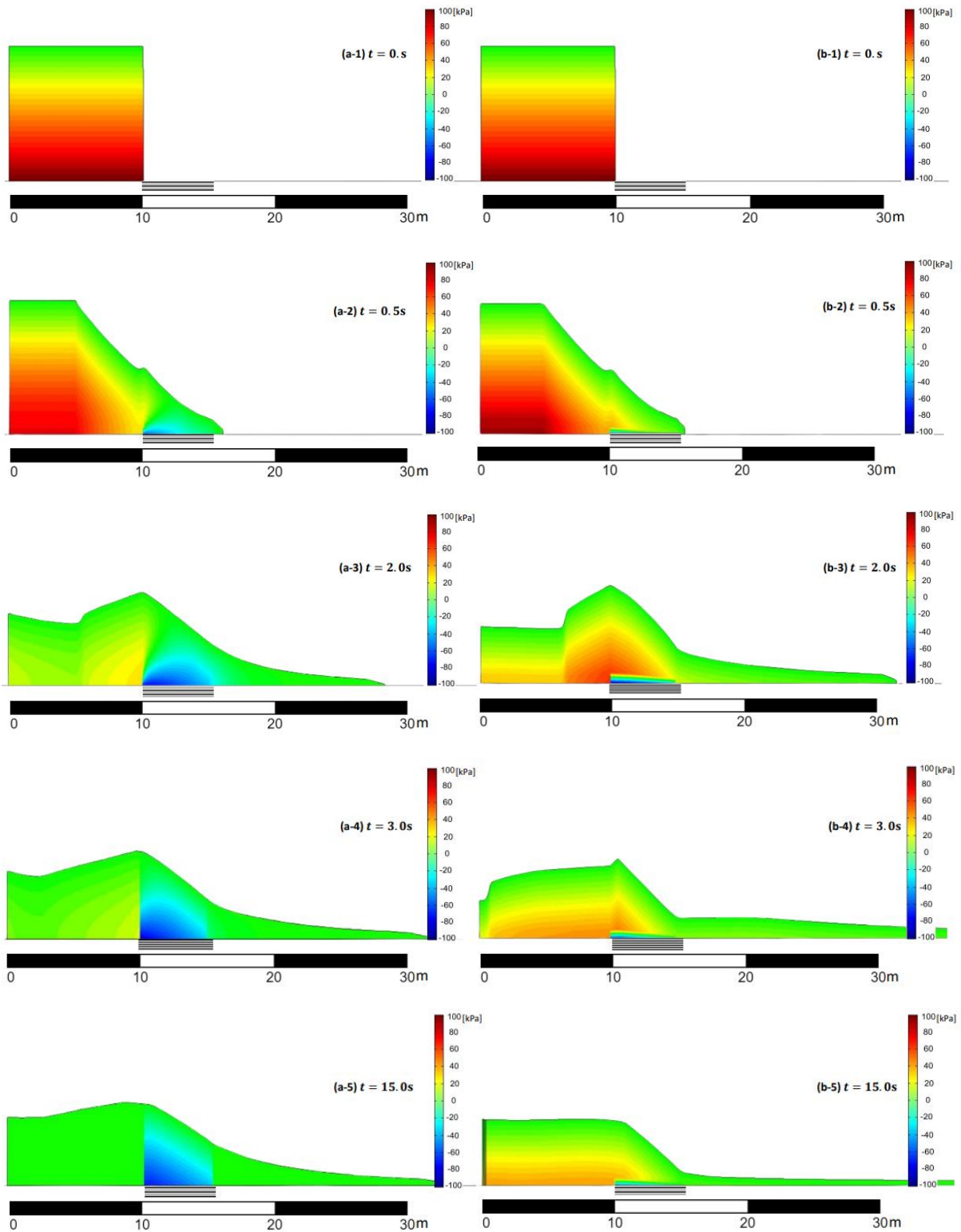
Figure 4.12: The distributions of excess pore-water pressure corresponding to dam break problems with (a) high and (b) low soil permeability.

By applying the SPH-FD model, it was possible to evaluate how installing the bottom drainage screens can dissipate significant energy and reduce the runout distance of debris flows consisting of low or high soil permeability. The numerical results show the capability of the presented model to properly reproduce the complex behaviour of debris flows propagating over permeable bottom boundaries, taking into account (i) pore-water pressures, (ii) porosity variations, and (iii) dewatering effects. Therefore, the proposed approach can be considered to assess the performance of this type of mitigation measure.

5 Application to a real case

5.1 Introduction

In this chapter, we will conduct a numerical analysis for a real case involving a landslide event in Favazzina, a part of Scilla municipality in the province of Reggio Calabria. To accurately model landslides, it is essential to consider erosion processes and their interaction with slope stability. Therefore, a simple erosion law is implemented to represent the bed entrainment phenomenon. At last, our analysis will focus on placing bottom drainage screens at different locations.

5.2 Bed entrainment

Bed entrainment, also called basal erosion, is a process which causes an increase in landslide volume due to the inclusion of soil, debris and trees uprooted from the ground surface during flow propagation [38]. Entrainment of material, located along the landslide path, is outlined as a key factor in controlling the dynamics of landslides of a flow-like character as observed in many catastrophic landslides. Therefore, it is necessary to understand its dynamics and consider the entrainment effects on runout analysis results.

The key parameter in evaluating the entrainment process is called entrainment rate (e_R) which is defined as the derivative of the ground surface elevation (z) with respect to the flow propagation time:

$$e_R = -\frac{\partial z}{\partial t} \tag{5.1}$$

which is generally agreed that the entrainment is positive if the elevation of ground surface diminishes [9].

Here, a simple law already implemented in the GeoFlow-SPH code, called Hungr's law will be described. Hungr's erosion law [15] assumes that the total volume of debris increases according to a specified rate. Therefore, the erosion rate (e_R) is defined as:

$$e_R = E_s.h.\bar{v} \tag{5.2}$$

which indicates a direct proportionality between the entrainment rate and the product of depth average velocity ($\bar{v}$) and mobilized soil depth (h). The landslide growth rate (E_s) can be obtained directly from the initial volume entering the erosion zone (V_0), final volume exiting the erosion zone (V_f) and the path length of the erosion zone (l) as:

$$E_s = \frac{\ln\left(\frac{V_f}{V_0}\right)}{l} \tag{5.3}$$

5.3 Case study

Our case study is a landslide event in Favazzina, part of the Scilla municipality in the province of Reggio Calabria. The study area, of about 1 km^2, is located on the south-western coast of the province of Reggio Calabria, in the hamlet of Favazzina in the municipality of Scilla. The area of interest is delimited by a mountainous region approximately 600 meters above sea level and the centre of Favazzina (fig. 5.1).
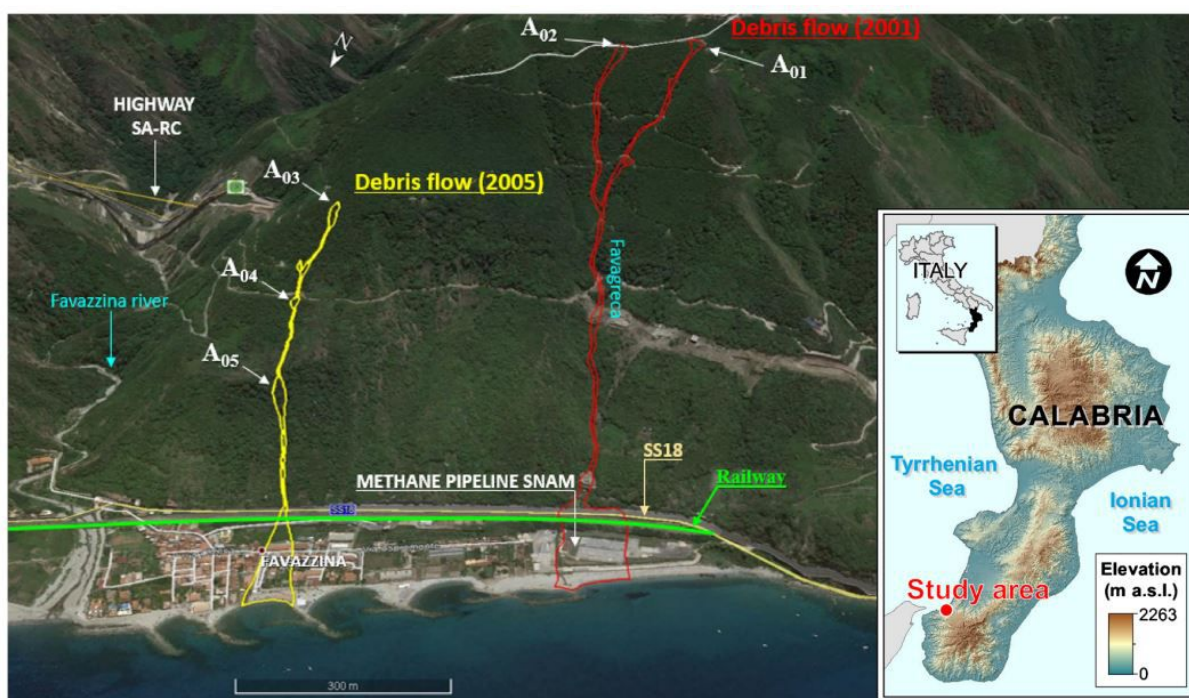
Figure 5.1: 2001 and 2005 debris flows in Favazzina [8]

It is worthwhile to mention that, two significant landslide events recorded in the area occurred in May 2001 and March 2005, causing extensive damage and involving various lifelines. The 2001 and 2005 debris flows initiated from the slide from a steep bank and are characterised by the small volume of the initiating slide; the bulk of the material involved in the debris flow events originated from entrainment from the path. This study focuses on the 2005 event, characterised by three translational shallow landslides (fig. 5.1), at about 370 m (triggering area A03), 242 m (triggering area A04) and 170 m a.s.l. (triggering area A05), respectively, that evolved into a debris flow. This debris flow caused serious damage to the transport infrastructures (the SS18 state road and the railway) and the derailment of the ICN Reggio Calabria-Milan intercity train [8].

5.4 Previous Studies

The event has been extensively studied previously [26, 8], and several numerical simulations using GeoFlow-SPH were performed, modeling the problem as single-phase with Bingham rheological behaviour. The choice to use this type of modeling was made under a series of specific site information and laboratory tests on the materials involved, such as viscometer tests and granulometric analyses. Thanks to the support of laboratory tests and subsequently through numerical modeling, it was possible to characterize the propagation process and identify the areas exposed to risk by determining the deposit area with a maximum accuracy of 92.5%. This demonstrates the adequacy of single-phase modeling with Bingham rheological law for the mentioned case. Additionally, two-phase modeling using Voellmy's rheological law yielded the same order of accuracy [42]. Therefore, we were confident in using the quantities provided by the noted works.

5.5 Back analysis

In this section, we will determine the parameters and conditions to reproduce the 2005 debris flow event. It involves working backward from the observed failure and deposition shape to estimate the initial conditions, material properties, and parameters that created the propagating mass.

Since we are required to model the event as a two-phase phenomenon, Voellmy's rheological law will be used. The results of calibrating parameters are shown in table 5.1.

SPH Data Input		
Parameters	**Index**	**Value**
Density of solid mass	ρ_s	2700 kg/m^3
Density of fluid	ρ_w	1000 kg/ m^3
Solid volume fraction	C_v	57%
Hydraulic conductivity (Modeling as Anderson and Jackson law)	$\bar{k}_w$	1.80×10^{-5} m/s
Basal friction angle	Φ_B	39°
Vertical Stiffness	E_v	60 MPa
Erosion Coefficient (Modeled in the code as Hungr's law)	E_s	0.00015 m^{-1}
Pore-water pressure ratio (To consider complete liquefaction)	R_u	1

Table 5.1: Calibrated quantities and parameters [42]

The initial landslide volumes and deposition shape (highlighted in white) are depicted in figure 5.2.
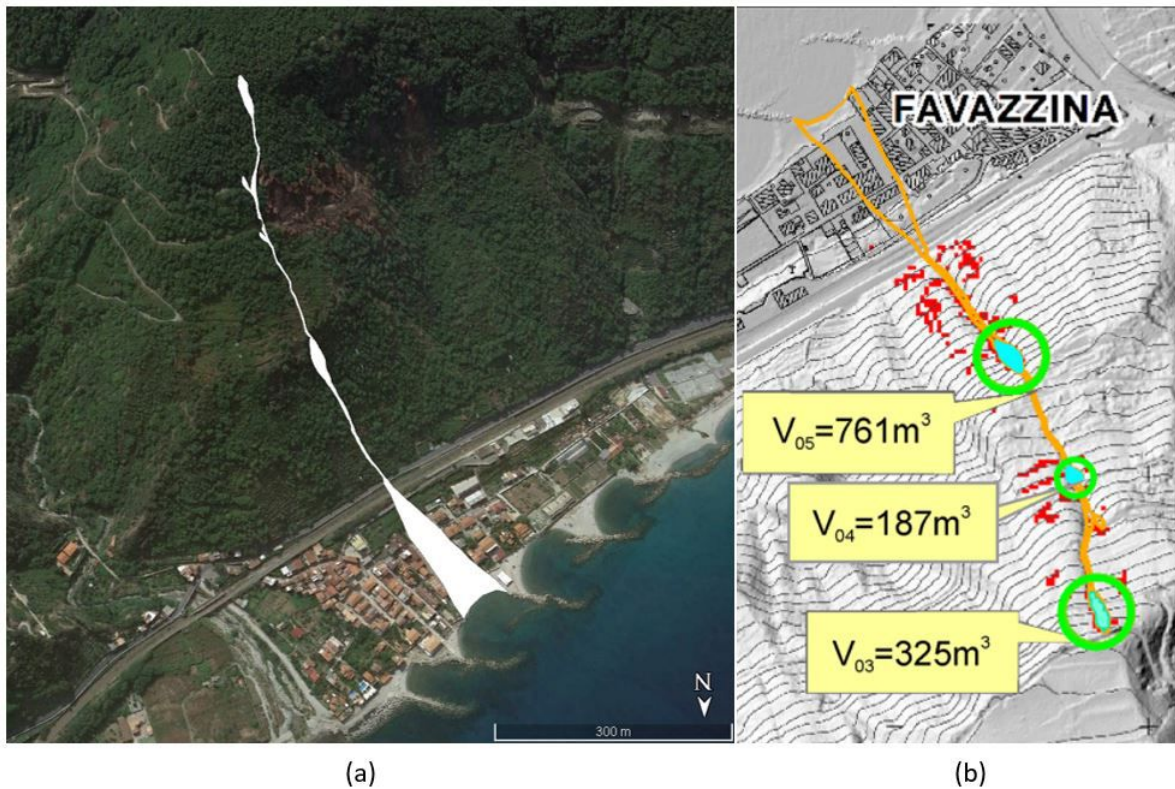
Figure 5.2: (a) Debris flow deposition on the real map , (b) Detached volumes [8]

For the simulation, source points have been defined in the areas of detatchment. It is essential to note that simulations are based on Digital Terrain Model (DTM), in which all above-ground features like buildings, vegetation, and infrastructure are not considered. This may introduce some degree of error compared to the real event.

To get a better insight of the flow path and the debris flow evolution, the runout at different temporal intances are displayed in figure 5.3. As evident, our numerical model accurately approximates the behavior of real complicated phenomenon. This is due to the precise representation of the material properties, boundary conditions, and other relevant parameters. Moreover, it validates our modeling assumptions and the choice of constitutive and rheological models.

However, it is worthwhile to mention that geotechnical problems often involve inherent uncertainties due to natural variability and limitations in measurement techniques. Accounting for these uncertainties can be challenging, and in most cases, it may not be possible to precisely replicate the real event in the simulation.

Performing simulations like these allows us to determine the affected area and estimate economic, social, and environmental losses resulting from the damage. This may involve assessing the cost of infrastructure repairs, the impact on livelihoods, environmental degradation, or public health risks.
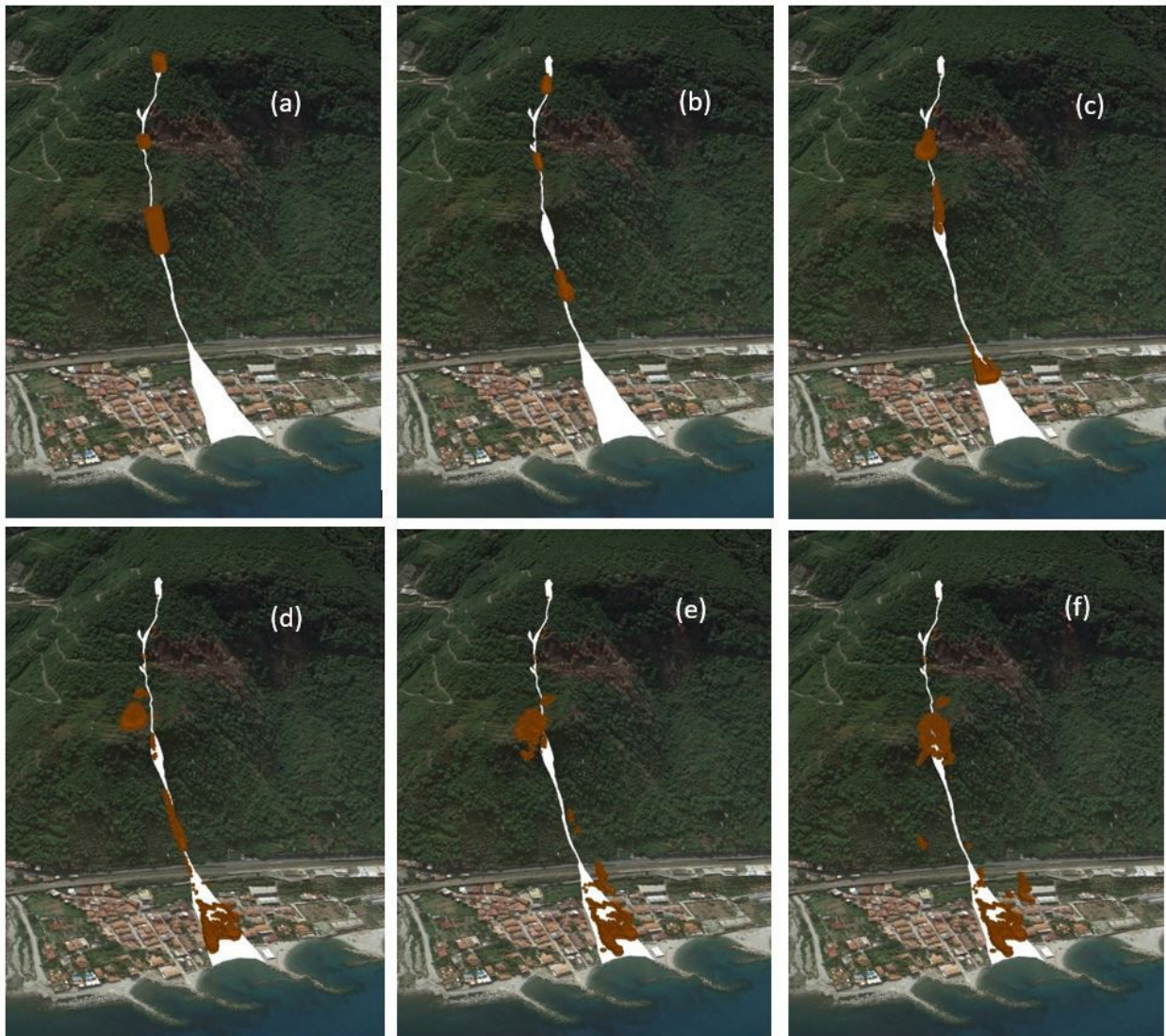
Figure 5.3: Debris flow evolution

5.6 Bottom drainage screens

As discussed in the previous chapter, bottom drainage screens can effectively dissipate energy and decrease the distance traveled by debris flows. When it comes to bottom drainage screen's slope, it is beneficial that it matches the slope of our terrain. This dramatically reduces impact forces and structural loads.

A screen with a length of 20m is placed at different locations so that more effective and efficient designs can be developed. As illustrated in figure 5.4, according to slope discontinuities along the propagation path, we consider four spots (A, B, C, or D) to position the screen. Moreover, two basal screens are strategically placed at the toe of a slope (C and D), where potential landslide material is expected to accumulate. Following that, we can compare the runout in each case to find the optimal location.

The deposition shape related to each case can be seen in figure 5.5.

Figure 5.4: Location of the screens

The kinetic energy of landslides is influenced by two crucial factors: velocity and volume. Landslides with high velocities and large volumes can cause widespread devastation and loss of life. The destructive power of such landslides is attributed to their ability to displace structures, erode the landscape, and bury everything in their path. To assess the extent of damage to infrastructure and buildings, a checkpoint is considered along the flow path and just before the urban area (fig. 5.6). This is to record the velocity and flow discharge. The volume traveled beyond the checkpoint was calculated by integrating the discharge over time.

The results are summarized in table 5.2. It can be observed that screens at A and B, would not reduce the magnitude of the very first impact and only decrease the passed volume. However, screens at point C and point D decrease flow velocity and volume. Between all four spots, point C seems to be the optimal location for setting up the screen. To further limit the affected area, two screens are placed at points C and D. This combination stops the flow before it reaches the urban area.
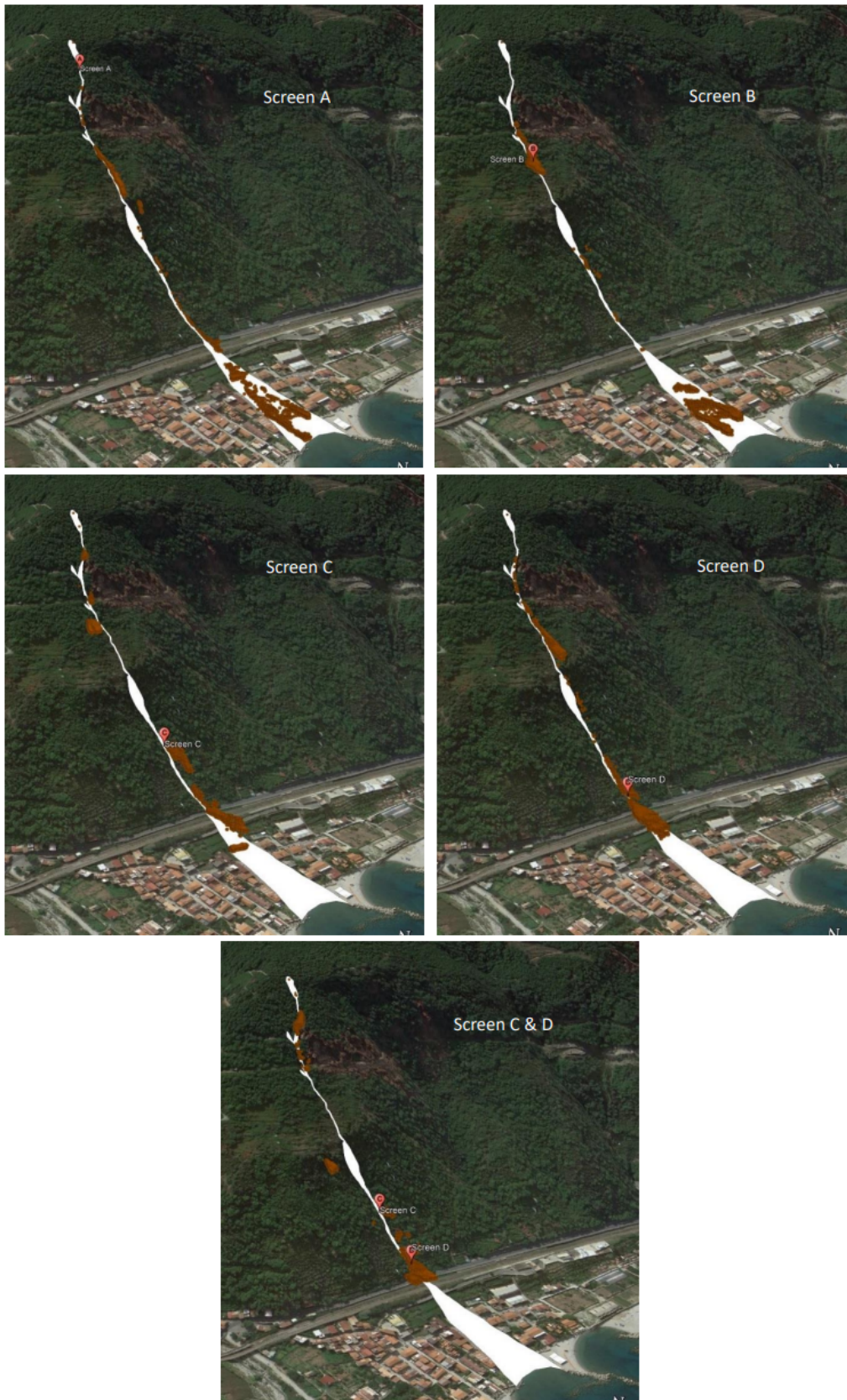
Figure 5.5: Screens' location and their corresponding runout

Figure 5.6: Specified checkpoint to record data

Screen	Ratio of Volume Passed	Volume Passed [m³]	Velocity [m/s]
No	0.75	960.5	40.1
A	0.72	914.1	40.1
B	0.57	723.6	40.1
C	0.42	534.7	26.8
D	0.53	676.1	29.3
C & D	0.27	346.3	18.2

Table 5.2: Volume and propagation velocity of the debris flow measured at the checkpoint

5.7 Some considerations

The effectiveness of a basal screen in reducing the runout distance of a landslide depends on various factors, including the characteristics of the slope, the magnitude of

the landslide, and the design and construction quality of the screen itself. Detailed engineering analysis and design are typically required to determine the appropriate dimensions, materials, and construction techniques for a basal screen in a specific landslide-prone area.

It's important to note that while basal screens can help mitigate the impact of landslides, they are not always a standalone solution. They are often implemented as part of a comprehensive slope stabilization and landslide risk management strategy, which may include other measures such as slope reinforcement, drainage improvements, or vegetation management. They can also complement other structural countermeasures like retaining walls and earthen embankments.

6 Conclusion

This M.Sc. thesis implements a depth-integrated two-phase SPH model for replicating the dynamics of debris flows. Debris flows are rapid landslides characterized by the movement of fluidized geomaterials. Understanding the evolution of excess pore-water pressure is crucial in studying debris flow behavior. The thesis is divided into five chapters, each covering specific aspects of the research.

Chapter 1 provides a brief introduction to rapid landslides, particularly debris flows, emphasizing the importance of considering the time-space evolution of excess pore-water pressure.

Chapter 2 introduces the two-phase mathematical model, which includes excess pore pressure in debris flows, specifically those consisting of low to medium permeable soils. This involves incorporating a one-dimensional consolidation equation into the system of equations. This chapter also presents two numerical methods to transform partial differential equations into ordinary differential equations. The mass and momentum balance equations are discretized using SPH, while the consolidation equation is discretized using a set of finite difference meshes associated with each SPH node representing a solid particle.

Chapter 3 explores different rheological laws to describe the behavior of fluidized geomaterials. Depth-integrated rheological relations are then presented to complete the governing equations discussed in Chapter 2. Additionally, several parametrical analyses have been performed to identify the factors that have a significant impact on the flow propagation.

Chapter 4 demonstrates the performance of the proposed two-phase SPH model. The model is used to investigate the role of excess pore-water pressure during debris flow propagation. Moreover, several sensitivity analyses are conducted within this chapter to provide valuable information regarding the influence of soil stiffness and permeability on runout distance and excess pore pressure evolution. The chapter concludes by performing additional analyses to assess the effectiveness of drainage screens in debris flows under different consolidation rates.

In Chapter 5, a real-life case study in Italy (Favazzina, 2005) is investigated. The case is selected based on reliable information, including topography, volume of the landslide, distribution of deposition, final runout, and estimated velocities. The results indicate that the proposed model is suitable for analyzing and forecasting debris flow propagation and deposition. As a mitigation measure, bottom drainage screens have been placed at different spots to reduce the potential damage caused by landslides.

Overall, this numerical model proved to be beneficial as a valuable tool for predicting the potential hazards associated with debris flows and can help researchers and practitioners make informed decisions regarding mitigation measures.

Bibliography

[1] T. B. Anderson and R. Jackson. Fluid Mechanical Description of Fluidized Beds. Equations of Motion. *Ind. Eng. Chem. Fundam.*, 6(4):527–539, nov 1967.

[2] Santiago Beguería, Th WJ Van Asch, J-P Malet, and S Gröndahl. A gis-based numerical model for simulating the kinematics of mud and debris flows over complex terrain. *Natural Hazards and Earth System Sciences*, 9(6):1897–1909, 2009.

[3] E. C. Bingham. *Fluidity and plasticity*. McGraw-Hill, New York, 1922.

[4] E. C. Bingham and H. Green. Paint, A Plastic Material and Not a Viscous Liquid, The Measurement of Its Mobility and Yield Value. *Proc. Am. Soc. Test. Mater.*, 19:640–664, 1919.

[5] Matteo Bonacina. Statale 36, macigni franano sulla lecco-ballabio. auto colpita, due "miracolati". `https://www.leccotoday.it/cronaca/statale-36-macigni-frana-sulla-lecco-ballabio-.html`, 2022.

[6] L. Cascini, S. Cuomo, M. Pastor, and I. Rendina. SPH-FDM propagation and pore water pressure modelling for debris flows in flume tests. *Eng. Geol.*, 213:74–83, nov 2016.

[7] M. Christen, J. Kowalski, and P. Bartelt. RAMMS: Numerical simulation of dense snow avalanches in three-dimensional terrain. *Cold Reg. Sci. Technol.*, 63(1-2):1–14, aug 2010.

[8] Mariantonietta Ciurleo, Mandaglio Mc, and NICOLA MORACI. A quantitative approach for debris flow inception and propagation analysis in the lead up to risk management. *Landslides*, 18, 02 2021.

[9] Sabatino Cuomo, Manuel Pastor, Vittoria Capobianco, and Leonardo Cascini. Modelling the space–time evolution of bed entrainment for flow-like landslides. *Eng. Geol.*, 212:10–20, sep 2016.

[10] Richard Davies. Flooding in northern italy, august 2022. `https://www.efas.eu/en/news/flooding-northern-italy-august-2022`, 2022.

[11] Vigili del Fuoco editorial staff. Italy's institutional agency for fire and rescue service. `https://twitter.com/vigilidelfuoco`.

[12] 3BMeteo editorial staff. Cronaca meteo ischia casamicciola: il video dal drone dove è nata la frana. `https://twitter.com/3bmeteo`, 2022.

[13] R. A. Gingold and J. J. Monaghan. Smoothed particle hydrodynamics - Theory and application to non-spherical stars. *Mon. Not. R. Astron. Soc.*, 181:375–389, 1977.

[14] Y. Gonda. Function of a debris-flow brake. *Int. J. Eros. Control Eng.*, 2(1):15–21, 2009.

[15] O. Hungr, S. McDougall, and M. Bovis. Entrainment of material by debris flows. In *Debris-flow Hazards Relat. Phenom.*, pages 135–158. Springer Berlin Heidelberg, Berlin, Heidelberg, 2005.

[16] K. Hutter, Y. Wang, and S. P. Pudasaini. The Savage–Hutter avalanche model: how far can it be pushed? *Philos. Trans. R. Soc. A Math. Phys. Eng. Sci.*, 363(1832):1507–1528, jul 2005.

[17] Overview Of Instability In Italy. Riskydrogeo project. `http://www.risknat.org/projets/riskydrogeo/docs/guide_pratique/Acivite1_Ateliers/Presentations%20Atelier1/A1P13-Coastal%20changes/programs/overitaly.html`, 2017.

[18] Y. Kim. *Study on Hydraulic Characteristics of Debris Flow Breakers and Sabo Dams with a Flap*. PhD thesis, Kyoto University, 2013.

[19] L. B. Lucy. A numerical approach to the testing of the fission hypothesis. *Astron. J.*, 82:1013–1024, 1977.

[20] S. McDougall and O. Hungr. A model for the analysis of rapid landslide motion across three-dimensional terrain. *Can. Geotech. J.*, 41(6):1084–1097, dec 2004.

[21] Scott McDougall. *A new continuum dynamic model for the analysis of extremely rapid landslide motion across complex 3D terrain*. PhD thesis, University of British Columbia, 2006.

[22] M. Mergili, J. Fischer, J. Krenn, and S.P. Pudasaini. r.avaflow v1, an advanced open-source computational framework for the propagation and interaction of two-phase mass flows. *Geosci. Model Dev.*, 10(2):553–569, feb 2017.

[23] J. J. Monaghan. Smoothed Particle Hydrodynamics. *Annu. Rev. Astron. Astrophys.*, 30(1):543–574, sep 1992.

[24] J. J. Monaghan. SPH without a Tensile Instability. *J. Comput. Phys.*, 159(2):290–311, apr 2000.

[25] J. J. Monaghan and R. A. Gingold. Shock simulation by the particle method SPH. *J. Comput. Phys.*, 52(2):374–389, nov 1983.

[26] NICOLA MORACI, Mandaglio Mc, Domenico Gioffre, and Antonia Pitasi. Debris flow susceptibility zoning: An approach applied to a study area. *Rivista Italiana di Geotecnica*, 51, 01 2017.

[27] Saeid Moussavi Tayyebi. *A two-phase SPH depth integrated model for debris flow propagation considering pore water pressure evolution*. PhD thesis, Universidad Politécnica de Madrid, 2019.

[28] James S O'Brien, Pierre Y Julien, and WT Fullerton. Two-dimensional water flood and mudflow simulation. *Journal of hydraulic engineering*, 119(2):244–261, 1993.

[29] Johnnatan Palacio, Martin Mergili, and Edier Aristizábal. Probabilistic landslide susceptibility analysis in tropical mountainous terrain using the physically based r.slope.stability model. *Natural Hazards and Earth System Sciences*, 20:815–829, 03 2020.

[30] M. Pastor, T. Blanc, B. Haddad, V. Drempetic, M. S. Morles, P. Dutto, M. M. Stickle, P. Mira, and J. A. Merodo. Depth Averaged Models for Fast Landslide Propagation: Mathematical, Rheological and Numerical Aspects. *Arch. Comput. Methods Eng.*, 22(1):67–104, jan 2015.

[31] M. Pastor, T. Blanc, and M. J. Pastor. A depth-integrated viscoplastic model for dilatant saturated cohesive-frictional fluidized mixtures: Application to fast catastrophic landslides. *J. Nonnewton. Fluid Mech.*, 158(1-3):142–153, may 2009.

[32] M. Pastor, M. Quecedo, E. Gonzalez, M. I. Herreros, J. A. Merodo, and P. Mira. Modelling of Landslides: (II) Propagation. In Félix Darve and Ioannis Vardoulakis, editors, *Degrad. Instab. Geomaterials*, pages 319–367. Springer Vienna, Vienna, 2004.

[33] M. Pastor, M. M. Stickle, P. Dutto, P. Mira, J. A. Fernández Merodo, T. Blanc, S. Sancho, and A. S. Benítez. A viscoplastic approach to the behaviour of fluidized geomaterials with application to fast landslides. *Contin. Mech. Thermodyn.*, 27(1-2):21–47, jan 2015.

[34] M. Pastor, A. Yague, M. M. Stickle, D. Manzanal, and P. Mira. A two-phase SPH model for debris flow propagation. *Int. J. Numer. Anal. Methods Geomech.*, 42(3):418–448, feb 2018.

[35] Manuel Pastor, Saeid M. Tayyebi, Miguel M. Stickle, Ángel Yagüe, Miguel Molinos, Pedro Navas, and Diego Manzanal. A depth integrated, coupled, two-phase model for debris flow propagation. *Acta Geotech.*, 16(8):2409–2433, aug 2021.

[36] E. B. Pitman and L. Le. A two-fluid model for avalanche and debris flows. *Philos. Trans. R. Soc. A Math. Phys. Eng. Sci.*, 363(1832):1573–1601, jul 2005.

[37] M. Rodriguez-Paz and J. Bonet. A corrected smooth particle hydrodynamics formulation of the shallow-water equations. *Comput. Struct.*, 83(17-18):1396–1410, jun 2005.

[38] S. B. Savage and K. Hutter. The dynamics of avalanches of granular materials from initiation to runout. Part I: Analysis. *Acta Mech.*, 86(1-4):201–223, mar 1991.

[39] S. M. Tayyebi, M. Pastor, and M. Stickle. Two-phase SPH numerical study of pore-water pressure effect on debris flows mobility: Yu Tung debris flow. *Comput. Geotech.*, 132:103973, apr 2021.

[40] Saeid Moussavi Tayyebi, Manuel Pastor, Andrei Hernandez, Lingang Gao, Miguel Martin Stickle, Ashenafi Lulseged Yifru, and Vikas Thakur. Two-Phase Two-Layer Depth-Integrated SPH-FD Model: Application to Lahars and Debris Flows. *Land*, 11(10):1629, sep 2022.

[41] David J Varnes. Slope movement types and processes. *Special report*, 176:11–33, 1978.

[42] Pasquale VISALLI. *Flow-type landslides: Propagation process and mitigation works modelling with a two-phase SPH depth-integrated method*. PhD thesis, University of Messina, Messina, Italy, 2023.

[43] A. L. Yifru, E. Laache, H. Norem, S. Nordal, and V. K. Thakur. Laboratory investigation of performance of a screen type debris-flow countermeasure. *HKIE Trans.*, 25(2):129–144, apr 2018.

[44] Ashenafi Lulseged Yifru. *Investigation of a screen structure for mitigating debris-flows along coastal roads*. PhD thesis, Norwegian University of Science and Technology, Trondheim, Norway, 2020.

[45] O. C. Zienkiewicz, A. H. C. Chan, M. Pastor, D. K. Paul, and T. Shiomi. Static and Dynamic Behaviour of Soils: A Rational Approach to Quantitative Solutions. I. Fully Saturated Problems. *Proc. R. Soc. A Math. Phys. Eng. Sci.*, 429(1877):285–309, jun 1990.

[46] O. C. Zienkiewicz, A. H. C. Chan, M Pastor, B. A Shrefler, and T. Shiomi. *Computational Geomechanics with Special Reference to Earthquake Engineering*. Wiley, 1st edition, 1999.

[47] O. C. Zienkiewicz and T. Shiomi. Dynamic behaviour of saturated porous media; The generalized Biot formulation and its numerical solution. *Int. J. Numer. Anal. Methods Geomech.*, 8(1):71–96, jan 1984.